TÉCNICO LISBOA

Isolated Matrix Converter for Interconnection of Low Voltage AC Grids to DC Grids

Bárbara Miguel Machado Cosme

Thesis to obtain the Master of Science Degree in

Electrical and Computer Engineering

Supervisors: Prof. Sónia Maria Nunes dos Santos Paulo Ferreira Pinto
Prof. José Fernando Alves da Silva

Examination Committee

Chairperson: Prof. Célia Maria Santos Cardoso de Jesus
Supervisor: Prof. Sónia Maria Nunes dos Santos Paulo Ferreira Pinto
Member of the Committee: Prof. Vitor Manuel de Carvalho Fernão Pires

January 2021

I declare that this document is an original work of my own authorship and that it fulfills all the requirements of the Code of Conduct and Good Practices of the Universidade de Lisboa.

Declaro que o presente documento é um trabalho original da minha autoria e que cumpre todos os requisitos do Código de Conduta e Boas Práticas da Universidade de Lisboa.

Finishing this dissertation represents the end of a five-year journey that would not have been possible without the support and help of some people who accompanied me throughout my journey at the Instituto Superior Técnico.

First of all, I would like to thank my mentors, especially Professor Sónia Pinto, for all the support and availability they have shown over the last few months, which have become crucial to the successful outcome of this work. Additionally, I would like to thank the project of the Fundação para a Ciência e a Tecnologia (FCT) PTDC/EEI-EEE/32550/2017 - Smart Transformers for Sustainable Grids, since it was within this project that the opportunity appeared to develop the topic of this dissertation.

I would also like to thank my family, especially my parents and my brother, for their support and patience with me throughout these years, particularly during the period of lockdown. Thank you for always being by my side and for providing me with everything I needed to become a better student.

Finally, I would like to thank all my friends who have been with me and marked over the past five years, not only for the friendship created but also for all the support and spirit of mutual help developed over the years, in particular to Ricardo Lameirinhas and Mariana Maldonado.

To everyone, thank you very much.

Abstract

With the technological advances of recent years, there has been a significant increase in DC operated equipment in the electrical grid, both in renewable energy sources and DC loads. The increasing use of this equipment in the network leads to a rethinking of the present network architecture. Is it still adequate or should it be complemented by a DC grid?

This dissertation proposes a bi-directional AC/DC converter to reduce network losses and make it more efficient, allowing the reduction of current and excessive conversion levels. Although this dissertation does not focus on the hybrid network, it focuses on one of its fundamental elements, the AC/DC converter, which allows interconnecting both parts of the grid. Therefore, the purpose of this work is to develop an isolated and bidirectional AC/DC matrix converter. To achieve this, it starts by defining the type of the converter and performing the sizing of its elements. The proposed system is composed of two matrix converters, a High-Frequency Transformer, and a DC/DC step-up converter.

The inclusion of this converter must ensure that disturbances in both networks are minimal, so a non-linear control system for DC grid voltage is developed, based on Lyapunov's stability theory.

Finally, Matlab's Simulink tool is used, and the system is simulated in several different scenarios. Through these simulations, it is possible to demonstrate that the system is bidirectional and that in all cases, the control system works correctly.

Keywords

Resumo

Com a evolução tecnológica dos últimos anos, tem-se observado um aumento significativo de equipamentos a operar em DC na rede electrica, seja em fontes de energia renováveis como em cargas DC. O aumento destes equipamentos na rede leva a repensar na atual arquitetura da rede. Será que esta ainda é adequada ou será que deve ser complementada por uma rede DC?

De forma a reduzir as perdas da rede e torná-la mais eficiente é proposto nesta dissertação um conversor AC/DC bidirecional, permitindo reduzir os atuais e excessivos níveis de conversão. Porém, esta dissertação não se foca na totalidade da rede híbrida, mas sim num dos seus elementos fundamentais, o conversor AC/DC que permite interligar ambas as partes da rede. Assim sendo, o objetivo deste trabalho é desenvolver um conversor matricial AC/DC, isolado e bidirecional. Para tal, começa-se por definir a tipologia do conversor e realizar o dimensionamento dos respetivos elementos. O sistema proposto é composto por dois conversores matriciais, um transformador de alta-frequência e ainda por um conversor elevador DC/DC.

A inclusão deste conversor tem de garantir que as perturbações em ambas as redes são mínimas, pelo que se desenvolve um sistema de controlo não linear para a tensão da rede DC, baseado na teoria da estabilidade de Lyapunov.

Por último, recorre-se à ferramenta Simulink do Matlab e efetua-se a simulação do sistema em vários cenários diferentes. Através destas simulações é possivel demonstrar que o sistema é bidirecional e que em todos os casos o sistema de controlo funciona corretamente.

Palavras Chave

Rede híbrida AC/DC; Conversor matricial AC/DC; Bidirecional; Transformador de alta frequência; Controlador não-linear.

x

Contents

List of Figures

Acronyms

AC   Alternating Current

DC   Direct Current

LED   Light-Emitting Diode

MC   Matrix Converter

IGBT   Insulated Gate Bipolar Transistor

SPMC   Single-Phase Matrix Converter

HFT   High Frequency Transformer

DCM   Discontinuous Conduction Mode

CCM   Continuous Conduction Mode

LSM   Lyapunov's Second Method

RMS   Root Mean Square

CPL   Constant Power Loads

EMI   Electromagnetic Interference

Nomenclature

$A(t)$ Command signal of $S_{11\,A}$ and $S_{22\,A}$ switches

$B(t)$ Command signal of $S_{12\,A}$ and $S_{21\,A}$ switches

C Boost converter capacitor

C_f Input filter capacitor

C_{cpl} Buck converter capacitor

D Boost converter diode

D_{cpl} Buck converter diode

$F(t)$ Command signal of $S_{11\,B}$ and $S_{22\,B}$ switches

$G(t)$ Command signal of $S_{12\,B}$ and $S_{21\,B}$ switches

$H(t)$ Intermediate function required to determine the $F(t)$ and $G(t)$ command signals

H_f Positive constant used in the input filter sizing

I_{DC} DC grid current source

I_{RMS} Root mean square of AC grid current

$I_{o_{cpl}}$ Constant Power Load output current

I_o DC grid current

I_o' Output current of the CPL input filter

K_I Backstepping integral control gain

K_v Backstepping voltage control gain

L Boost converter inductor

L_f Input filter inductor

L_m HFT magnetizing inductor

L_{T1} Inductor of HFT primary windings

L_{T2} Inductor of HFT secondary windings

L_{cpl} Buck converter inductor

$M(t)$ Intermediate function required to determine the $F(t)$ and $G(t)$ command signals

N_1 Number of turns of the HFT primary windings

N_2 Number of turns of the HFT secondary windings

P_o DC grid power

P_{cpl} Constant Power Load power

P_{grid} Apparent AC grid power

R_f Input filter resistor

R_m HFT magnetizing resistance

R_o Equivalent DC grid resistance

R_{T1} Resistance of HFT primary windings

R_{T2} Resistance of HFT secondary windings

R_{cpl} Buck converter resistor

S Boost converter semiconductor

S_{cpl} Buck converter semiconductor

S_{kj} Bi-directional switch connecting output k to input j of a matrix converter

T AC grid Time period

T_s Switching time period

$V(x)$ Lyapunov function

V_M Maximum AC grid voltage

V_{RMS} Root mean square of AC grid voltage

$V_{o\,av}$ DC grid average voltage

$V_{o_{cpl}}$ Constant Power Load output voltage

V_o DC grid voltage

V_o' Output voltage of the CPL input filter

X_{pu} Variable X in pu values

X_{ref} Reference of the X variable

Y Rectified sinusoid, with maximum unitary amplitude and synchronous with the AC grid

Z_f Characteristic impedance of the LC filter

ΔQ Electric charge variation

ΔX Ripple of the X variable

Δ Bandwidth

δ Duty-cycle

γ Boost converter operation mode

γ_{cpl} Buck converter operation mode

ζ Damping factor

e_X Control error of the X variable

$e_{I_{cpl}}$ Control integral error of CPL output voltage

e_I Control integral error of DC grid voltage

f_c Cut-off frequency

f_s Switching frequency

$i_{L\,ref\,2}$ Boost converter inductor reference current (synchronous with the AC grid)

$i_{X\,av}$ Average current of the system X element

i_X Current of the system X element

i_{grid} AC grid current

i_p Current flowing between the AC/AC converter output and the primary of the High Frequency Transformer

i_s Current flowing between the secondary of the High Frequency Transformer and the AC/DC converter input

i_x Current flowing between AC/DC converter output and boost converter input

p_{dc} Instantaneous DC grid power

p_{grid} Instantaneous AC grid power

r_i Negative incremental resistance

$s(x)$ Sliding surface

t_i Instant of time when switching on the control signal of the matrix converter occurs

$v_{X\,av}$ Average voltage of the system X element

v_X Voltage of the system X element

v_{grid} AC grid voltage

v_p Primer voltage of the High Frequency Transformer

v_s Secondary voltage of the High Frequency Transformer

v_x AC/DC converter output voltage

w AC grid angular frequency

w_c Cut-off angle frequency

1

Introduction

Contents

1.1 Motivation

It has been over a hundred years since George Westinghouse and Nikolai Tesla won the famous "War of Currents" [1]. This "war" took place from around 1888 until 1891 and put two different energy supply systems face to face [2]. On one side was Thomas Edison with his Direct Current (DC) distribution system and on the other George Westinghouse and Nikolai Tesla with the Alternating Current (AC) system [1, 2]. The transformer's invention was the reason to the victory of the last system, as it allowed for a substantial reduction in energy transportation costs between distant AC generation plants and load centers [1, 2]. With the end of the "war", AC systems developed and expanded very quickly into a centralized, radial system, as shown in the leftmost diagram of figure 1.1 [2]. However, DC systems did not disappear completely, and nowadays, technological advances and the connection of new generation systems and electronic loads in the network lead to a rethinking of its architecture and the possibility of having DC grids in the near future. [2].

Over the years, there has been an evolution in the typology of loads. Conventional AC loads, such as washing machines, refrigerators, or air conditioners, are gradually changing and instead of having only one AC motor, they are also starting to include an AC/DC converter to minimize consumption and consequently save energy [2, 3]. Furthermore, in our daily life, we are increasingly surrounded by DC loads, whether at home, in the office, or on the street, with televisions, laptop computers, mobile phones, Light-Emitting Diode (LED) lighting, electric vehicles being examples of these DC loads [3, 4]. However, it is necessary to add AC/DC converters to connect the DC loads to the AC grid.
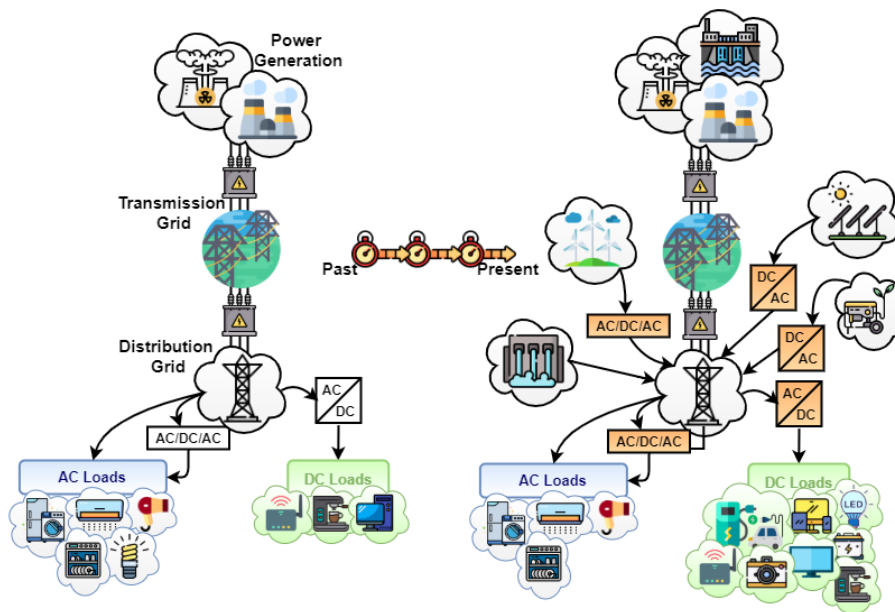
Figure 1.1: Evolution of network architecture over the years (based on [2] and the icons are from [5]).

In recent years, global warming and the limited fossil resources have stimulated the use of renewable energy sources, which has caused changes in the architecture of the network, as presented in the second diagram of figure 1.1 [2]. As a result, the system is decentralized, and the power flow is now bidirectional in the distribution network. Photovoltaic panels, wind turbine generators, and fuel cell generators are some examples of renewable energy sources [2–4]. However, photovoltaic systems and fuel cell generators are operated in DC, so currently, to be connected to the AC grid, they need a DC/AC converter [3]. Moreover, wind turbine generators have an intermediate DC link so they can be directly connected to a DC network [3]. It then appears that the inclusion of renewable sources and the change in load typology has increased system losses due to the need to include several AC/DC or DC/AC converters [2]. Table 1.1 shows how many and which converters are needed, considering the types of system, source, and load.

Table 1.1: Types of conversion considering the type of system, source and load (adapted from [2]).

			Load		
			DC	**AC**	**AC + DC/AC conv.**
System	**AC**	**AC source**	AC/DC	no	AC/DC/AC
		DC source	DC/AC/DC	DC/AC	DC/AC/DC/AC
	DC	**AC source**	AC/DC	AC/DC/AC	AC/DC/AC
		DC source	DC/DC*	DC/AC	DC/AC

*exists when it is necessary to raise or reduce the voltage level

Table 1.1 shows that there will be very few or no conversion processes if the AC loads or generation systems are connected to an AC network and the DC loads or generation systems to a DC grid. Therefore, the solution proposed in this dissertation is to develop a AC/DC converter thus allowing to reduce the number of converters, increasing the overall efficiency of the system. Therefore, this dissertation focuses on defining a conversion system that allows interconnecting both networks efficiently, as presented in figure 1.2.
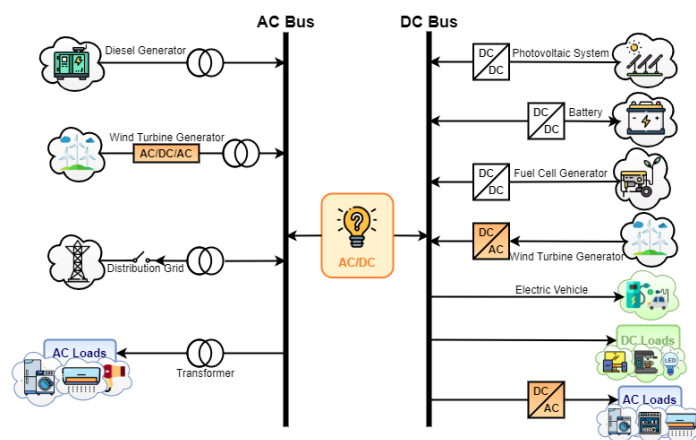
Figure 1.2: Solution proposed in this dissertation: an AC/DC hybrid system (based from [2, 4] and the icons are from [5]).

1.2 Objectives

The main objective of this dissertation is to develop a conversion system that allows connecting a low voltage single-phase AC network to a DC network. It is intended to have a bi-directional power flow in this converter and to have galvanic isolation to guarantee safety.

It is established several stages to ensure that the system meets all the proposed requirements and presents a desirable behavior. All these stages are developed throughout the dissertation.

The first step is to define the topology of the converter and size its components. Set the command system of the matrix converters considering their function. The next step is to define a control strategy for the DC voltage to guarantee minimum system disturbances.

Finally, the system simulation is performed, which includes the control system, using Matlab's Simulink. Several simulations are performed in different scenarios to analyze the system's behavior in various cases.

1.3 Outline

This thesis is divided into five chapters. The first chapter is the introduction of the project to be developed, where the motivation is presented and the objectives defined.

Chapter 2 introduces the proposed model of the bidirectional and isolated AC/DC matrix converter. Besides including a detailed study of the proposed system, it also contains the sizing of its filters.

In chapter 3, a non-linear control system based on the backstepping and sliding mode control theories is presented. For this purpose, both principles are presented theoretically and then applied to the proposed system.

In chapter 4, the simulation results, considering different scenarios, are presented and analyzed.

Finally, chapter 5 presents the overall conclusions and mentions some topics for future work to improve this study.

2

Proposed Solution

Contents

2.1 Proposed Solution

Selecting an appropriate typology for a converter is crucial to achieving all the proposed requirements [6]. However, today there is a wide variety of different topologies that allow the implementation of a single-phase, bi-directional, and isolated AC/DC converters [6]. As such, evaluating all the options is complex and extensive work [6]. Therefore, this chapter provides an introduction to the system proposed in this dissertation and a detailed analysis of each of the system components.

Figure 2.1 presents the solution proposed in this dissertation, an isolated matrix converter that allows connecting a single low voltage Alternating Current (AC) grid to a Direct Current (DC) grid.
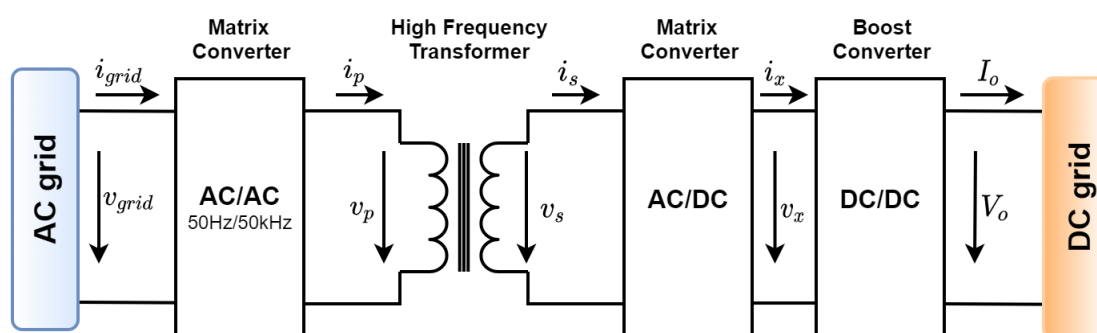
Figure 2.1: Proposed system diagram.

In figure 2.1, it can be seen from left to right, that is, from the AC grid to the DC grid, that the first component of the system is an AC/AC matrix converter. This converter aims to increase the frequency of the AC grid voltage to the switching frequency of the system. The second component of the system is a High Frequency Transformer (HFT), to guarantee galvanic isolation. Between the HFT and the DC network, the system features a second matrix converter, in this case, an AC/DC converter followed by a step-up converter. Together, these two converters have the function of converting the high frequency AC voltage into a DC voltage. However, it is intended to have a bi-directional system. Therefore, the power generated in the DC grid can be injected in the AC grid.

2.2 High Frequency Transformer

Since the introduction of AC systems in 1887, the magnetically coupled transformer has become an essential asset in the electrical grid, thus allowing voltage transformation and galvanic isolation [7]. Although the basic construction of the transformer has not undergone many changes in the last century, there has been a significant evolution in the processing of materials and the creation of new alloys with high magnetization densities and low hysteresis losses [7]. That has allowed the design of more efficient transformers to be operated at higher frequencies. [7].

This progress associated with the development of power electronic converters and advances in semi-conductor technology (faster switching capabilities, higher blocking voltages, and higher power densities) has allowed the creation of multi-functional equipment for applications in low voltage networks [8]. Thus, the HFT is expected to be able to replace the traditional 50/60 Hz transformer [8].

In this way, besides being galvanically insulated and having the capacity to reduce/increase the voltage value, it also allows intelligent energy management, power quality enhancement, low weight, low volume, and high energy density [9–11].

Figure 2.2 shows the location of the working frequency of the classic transformer versus the working frequency range of an HFT. While a conventional transformer operates between 50 and 60 Hz, the HFT generally has a work frequency range from several kilohertz to hundreds of kilohertz [12].
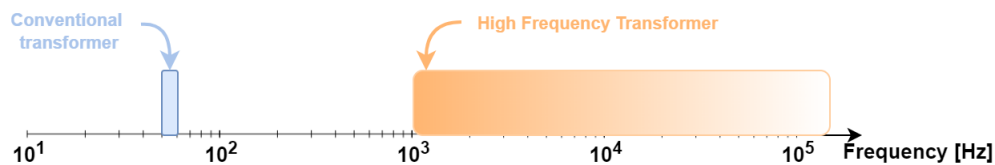
Figure 2.2: Graph of the working frequency of conventional transformer against the working frequency range of the HFT (adapted from [13]).

Figure 2.3 presents the equivalent Steinmetz model of a conventional transformer. This model not only includes the diagram of an ideal transformer with a transformation ratio, m, equal to N_2/N_1 but also considers the main non-idealities, with the inclusion of elements in the scheme that characterize its losses [14].
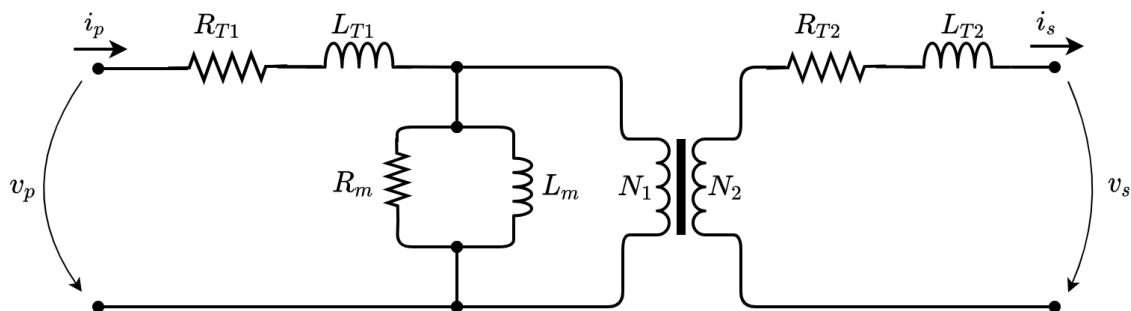
Figure 2.3: Equivalent scheme of a conventional transformer (adapted from [14]).

The losses in the copper windings are characterized by the R_{T1} and R_{T2} resistances and by the L_{T1} and L_{T2} inductances. While, R_m resistance represents the losses of the magnetization circuit in the transformer core [14].

If the analysis of the transformer is made using p.u. values, it is verified that the representation of the ideal transformer is unnecessary because the transformation ratio m becomes unitary [14]. There-

fore, figure 2.3 can be simplified, leading to figure 2.4, which presents the equivalent T diagram of a transformer.
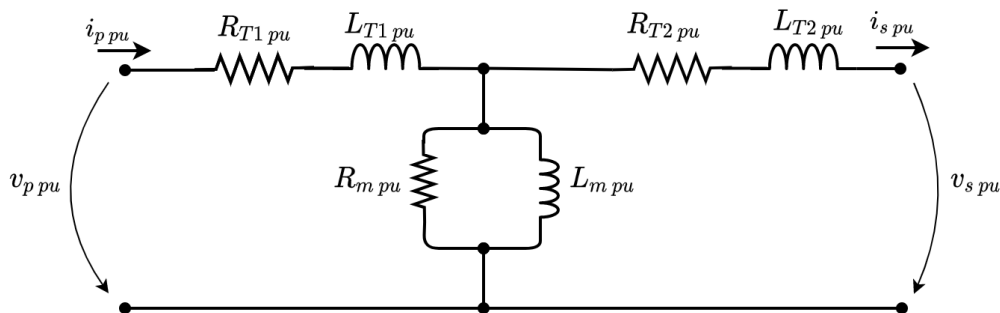
Figure 2.4: Equivalent T scheme of a transformer (adapted from [14]).

However, the system developed in this dissertation includes an HFT and not a conventional transformer, and the equivalent scheme described in figure 2.4 is used to represent it. However, it is applied a scale factor (related to the working frequency) in the sizing of the leakage and magnetizing inductances. All the steps concerning this sizing are described in Appendix A.

2.3 Matrix Converter

The concept of the Matrix Converter (MC) was first published in 1976 [15]. However, the name "matrix converter" appeared only in 1980, when Venturini and Alessina really developed the matrix converter, presenting the power circuit of a converter as a matrix of bidirectional power switches [16].

In recent decades, technological development has made it possible to create zones of operation at high frequencies, and at the same time, relatively low driving voltage drops [11, 17]. This progress, associated with an improvement in command and control circuits, has been the main responsible for the growing interest in matrix converters, with high frequency command [17].

One of the main advantages that distinguish it from other technologies is that it allows bi-directional power flow, although it has other benefits, as shown in figure 2.5 [15]. However, as this converter consists mostly of semiconductors, this makes the switching process between the various semiconductors more complex and makes it harder to define modulation strategies that guarantee both sinusoidal output voltages and input currents [17].
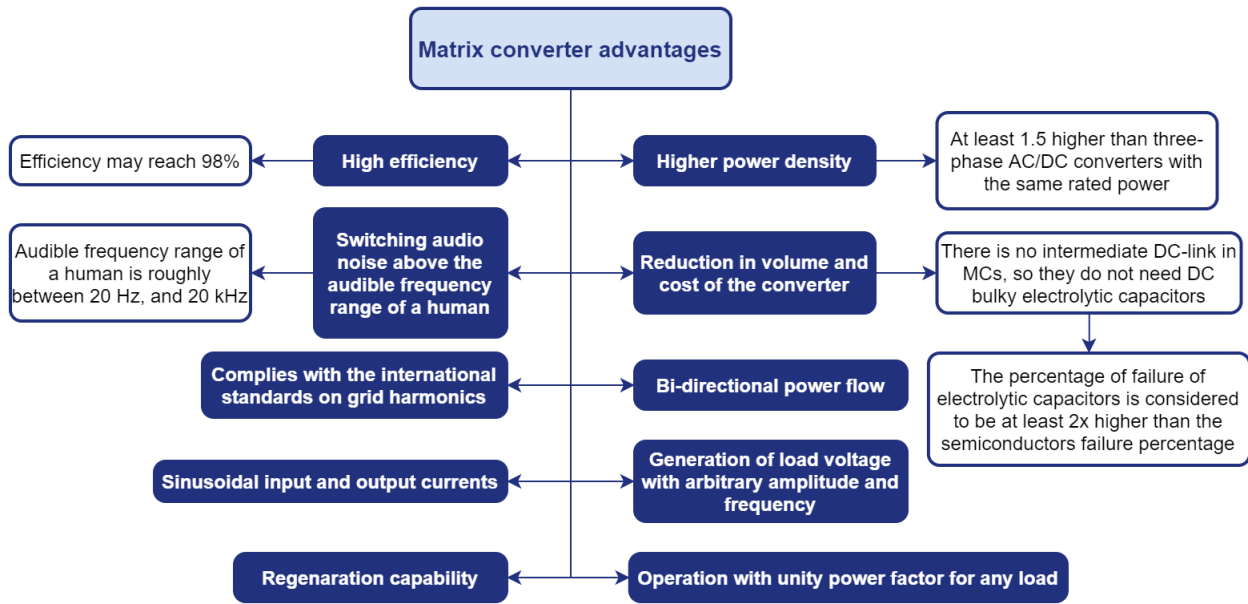
Figure 2.5: Diagram of MC advantages (information sourced on [11, 16–18]).

2.3.1 Matrix Converter Model

Figure 2.6a presents a generic model of an MC, which consists of a set $n \times m$ bi-directional power switches to connect, directly, an n - phase voltage source to an m - phase current source [17].

As each switch has two states, theoretically, this would allow $2^{n \times m}$ connection combinations [16]. However, voltage sources should not be short-circuited, and current sources should not be left open [17]. So, these topological constraints mean that a system with n voltage sources and m current sources can only have nm possible combinations [16, 17].

The MC requires a bi-directional switch capable of blocking voltage and conducting current in both directions [16]. Unfortunately, there are currently no semiconductors that meet these requirements, so it is necessary to build these switches with associations of semiconductors. [15, 16].

Figure 2.6b shows the solution used to solve this problem, which is the use of the common-emitter anti-parallel Insulated Gate Bipolar Transistor (IGBT), diode pair. In this way, the diode provides the switching module the reverse blocking capability, while the IGBT guarantees high-frequency switching capabilities [15].

9
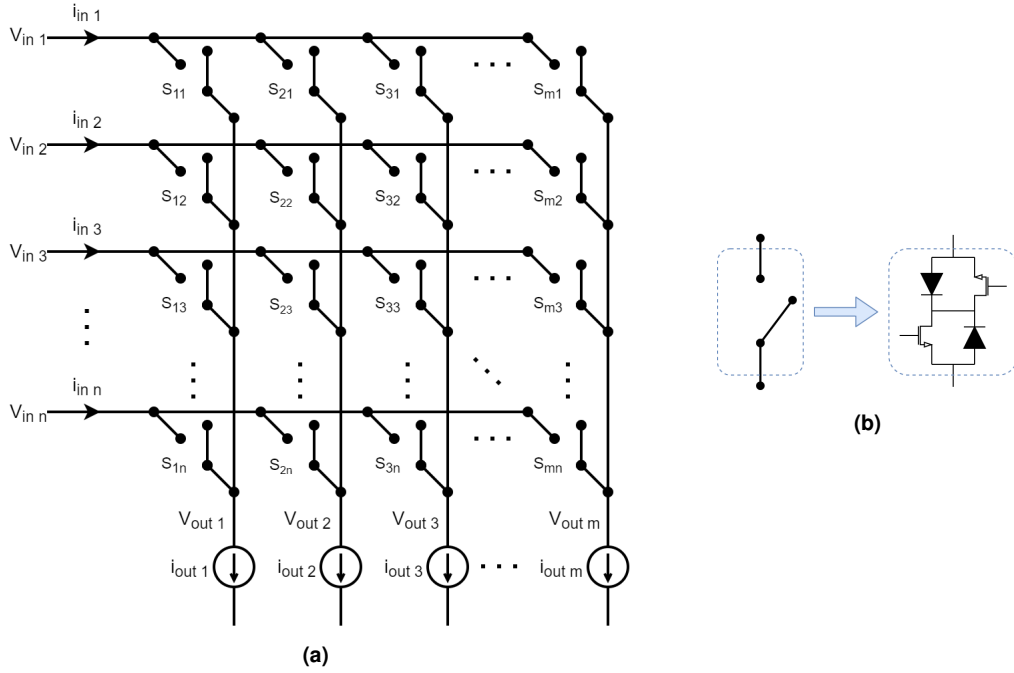
Figure 2.6: (a) Graphical representation of a MC with $n \times m$ phases (adapted from [17]); (b) Graphical representation of a bi-directional switch module (adapted from [11]).

Each bidirectional switch can be mathematically defined by a variable S_{kj}, assuming ideal semiconductors, which can assume two possible states: "$S_{kj} = 1$" if the switch is ON and "$S_{kj} = 0$" if the switch is OFF, as presented in the expression (2.1) [11, 17].

$$S_{kj} = \left\{ \begin{array}{ll} 1 & \text{, if switch is ON} \qquad k \in \{1, ..., m\} \\ 0 & \text{, if switch is OFF} \qquad j \in \{1, ..., n\} \end{array} \right. \tag{2.1}$$

2.3.2 Single-Phase Matrix Converter

The system under study in this thesis is a single-phase system, so the matrix converters that constitute the system are also Single-Phase Matrix Converter (SPMC)s. Zuckerberger was the first to develop this variant of matrix converter, and this matrix is formed by four bi-directional switches, as shown in figure 2.7 [19]. Besides, it is possible to represent the state of the semiconductors through a 2x2 matrix, as the one presented in expression (2.2) [19].
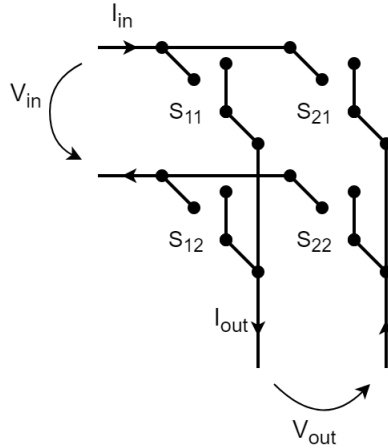
Figure 2.7: Graphical representation of a single-phase MC (adapted from [11]).

$$S = \left[\begin{array}{cc} S_{11} & S_{12} \\ S_{21} & S_{22} \end{array} \right] \tag{2.2}$$

Figure 2.1 shows that the converter under study includes two MCs. However, the functions that each one performs in the system are different. So, the switching strategy for each one is different. While the MC on the left in figure 2.1 is a direct AC/AC SPMC and aims to convert the AC mains voltage into a voltage with the same amplitude but switched at 50 kHz, the other MC (on the right in figure 2.1) is a direct AC/DC SPMC. This last SPMC aims to convert the voltage at the output of the HFT (switched at 50 kHz) into a rectified sinusoidal signal, with a frequency equal to the AC grid frequency.

The switching systems used in each of the converters are presented in detail below. Figure 2.8 shows the detailed diagram of each of the MC's under study, considering their location in the diagram in figure 2.1.

(a) AC/AC SPMC.

(b) AC/DC SPMC.
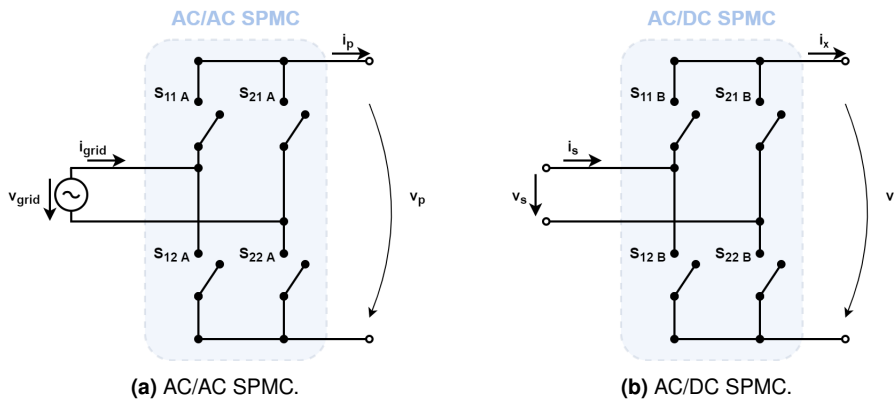
Figure 2.8: Detailed diagrams of the MCs that compose the system.

11

2.3.3 AC/AC Single-Phase Matrix Converter Switching Strategy

Typically, an MC is used as a voltage source-based converter system [20]. However, in the proposed approach the usual control strategies cannot be used because the converter is connected to a high frequency transformer and the average value of the voltage in each switching period must be zero to avoid the saturation of the transformer.

Table 2.1 presents the four possible switching states, considering the existing topological constraints. This means that it is not possible to have switches $S_{11\,A}$ and $S_{21\,A}$ or $S_{12\,A}$ and $S_{22\,A}$ conducting simultaneously to ensure that the AC network is not short-circuited. On the other hand, it is necessary to ensure that at least one of the $S_{11\,A}$-$S_{12\,A}$ and $S_{21\,A}$-$S_{22\,A}$ pair switches is conducting at every moment to guarantee the continuity of the output current.

Name	State	$S_{11\,A}$	$S_{12\,A}$	$S_{21\,A}$	$S_{22\,A}$	v_p
1	1	1	0	0	1	v_{grid}
2	-1	0	1	1	0	$-v_{grid}$
3	0	1	1	0	0	0
4	0	0	0	1	1	0

Table 2.1: Possible switching states of AC/AC SPMC.

Figure 2.9 presents the graphic sketch of the input and output signals to be obtained in this same converter to make explicit the purpose of the AC/AC SPMC. In other words, it is intended to convert a sinusoidal sign with a frequency of 50 Hz into another signal with the same amplitude but switched at 50 kHz. It is important to note that figure 2.9 is not to scale.
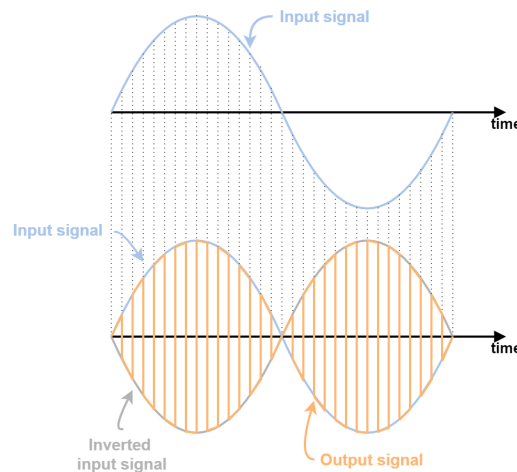
Figure 2.9: Graphical outline of desired input and output waveforms for AC/AC SPMC (it is not to scale).

Therefore, taking into account the waveform of the desired signals, as presented in figure 2.9, and the various possible switching states listed in table 2.1, it is possible to conclude that only the "1" and

"-1" situations are required to obtain the desired signal at the output. Hence, table 2.2 presents the commutation strategy for each of the switches, considering the desired output sign, for the first commutation periods.

Switching time	Intended output signal	$S_{11\,A}$	$S_{12\,A}$	$S_{21\,A}$	$S_{22\,A}$
0	v_{grid}	ON	OFF	OFF	ON
t_i	$-v_{grid}$	OFF	ON	ON	OFF
$2 \cdot t_i$	v_{grid}	ON	OFF	OFF	ON
$3 \cdot t_i$	$-v_{grid}$	OFF	ON	ON	OFF
$4 \cdot t_i$	v_{grid}	ON	OFF	OFF	ON

Table 2.2: Commutation strategy for each of the switches for the first commutation periods.

It is evident analyzing the data presented in table 2.2 that the switching strategy to be applied is the full-wave command. The full-wave command is a two-level command, where the switch pairs $S_{11\,A}$-$S_{22\,A}$, and $S_{12\,A}$-$S_{21\,A}$ are commanded in a complementary manner [17]. That is, during $T_s/2$, the switches $S_{11\,A}$ and $S_{22\,A}$ are commanded to drive, while $S_{12\,A}$ and $S_{21\,A}$ are commanded to cut-off. And, during the other half-period, $S_{12\,A}$ and $S_{21\,A}$ are set to drive, while $S_{11\,A}$ and $S_{22\,A}$ are set to cut-off [17].

Once the switching strategy to be used in the AC/AC matrix converter has been defined, the next step is to establish a solution that allows applying this same strategy in the system simulation. First, it is worth mentioning that to obtain more reliable results from the simulation, it is necessary to ensure that all the command signals applied to the system are synchronous. Therefore, to ensure synchronization between command signals, only one command signal is generated, and the remaining commands are created from this generated signal.

The proposed solution consists of generating a rectangular signal, $A(t)$, which switches between 0 and 1, at an f_s frequency, and with a 50% pulse width. This signal will thus be the command signal of switches $S_{11\,A}$ and $S_{22\,A}$. On the other hand, it is known that the command signal for $S_{12\,A}$ and $S_{21\,A}$ is inverse to the command described above. Thus, through the mathematical operations present in figure 2.10, it is possible to obtain the desired command signal, $B(t)$, for $S_{12\,A}$ and $S_{21\,A}$ through the command signal generated for $S_{11\,A}$ and $S_{22\,A}$.
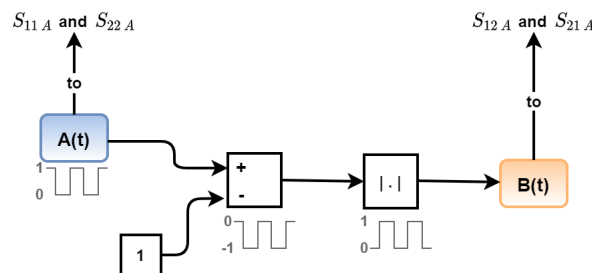
Figure 2.10: Graphical representation of the solution presented for the command signals of the AC/AC MC.

13

2.3.4 AC/DC Single-Phase Matrix Converter Switching Strategy

For the AC/DC matrix converter, the restrictions to the possible switching states, listed in the preceding section 2.3.3, also apply to this converter, and table 2.3 presents the four switching states of the AC/DC SPMC.

Name	State	S_{11}	S_{12}	S_{21}	S_{22}	v_x
1	1	1	0	0	1	v_s
2	-1	0	1	1	0	$-v_s$
3	0	1	1	0	0	0
4	0	0	0	1	1	0

Table 2.3: Possible switching states of AC/DC SPMC.

The purpose of this converter is to convert the current on the secondary side of the HFT into a synchronous, rectified sinusoidal current with the AC network, i.e., it is intended to have at the output of the converter a waveform current with only positive arcs. Figure 2.11 presents a scheme where the desired waveforms for the input and output waveforms are represented, and it is relevant to point out that the image is not at scale.
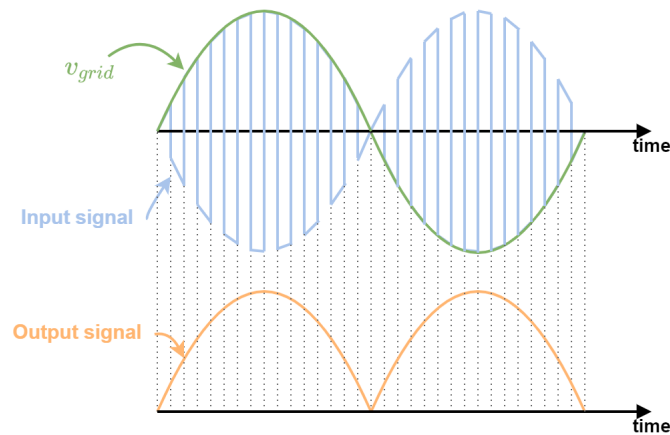
Figure 2.11: Graphical outline of desired input and output waveforms for AC/DC SPMC (it is not to scale).

This MC output waveform allows for the existence of a bi-directional flow as it enables converting the AC grid voltage into a continuous voltage by including a boost converter after this converter. On the other hand, it is possible through the DC grid voltage to recover the desired waveform to the AC grid voltage. In this way, it is possible to have both grids (AC and DC) waveforms without disturbances.

It is necessary to apply a modified full-wave command to achieve the results present in figure 2.11. That is, the common control in the full-wave is not enough because, in this case, it is necessary to consider the signal from the AC grid voltage so that a bi-directional flow is possible. Therefore, during $T/2$, the command signal is the same as described in the previous section and used in the AC/AC MC, whereas in the other half-period, the command signal is the symmetric of the previous one.

After the definition of the AC/DC matrix converter switching strategy, a solution is developed to implement this strategy in the system simulation. Therefore, we begin by defining the new command signals from the $A(t)$ command signal, described in section 2.3.3, to ensure synchronization between the command signals. After some mathematical operations and taking into account the AC grid voltage signal, the command signals $F(t)$ and $G(t)$ are obtained, which control the switch pairs $S_{11\,B}$-$S_{22\,B}$ and $S_{12\,B}$-$S_{21\,B}$, respectively. Figure 2.12 covers all the steps required to reach $F(t)$ and $G(t)$, including the intermediate functions $H(t)$ and $M(t)$.
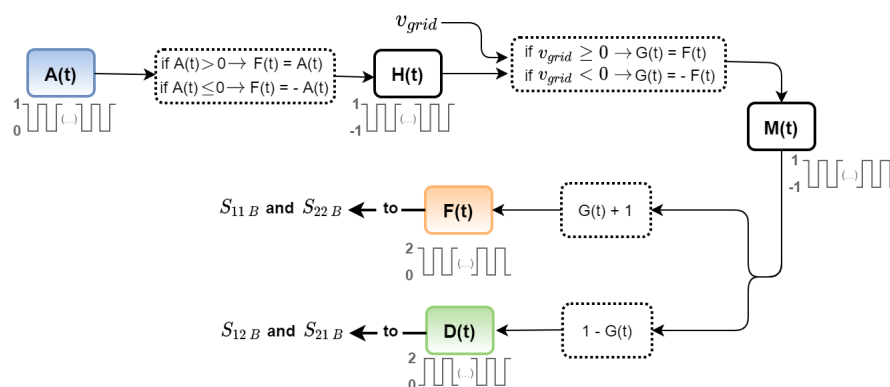
Figure 2.12: Graphical representation of the solution presented for the command signals of the AC/DC MC.

2.4 Step-Up Converter

The step-up converter, also known as a boost converter, is a type of DC/DC power converter, which, allows to raise the voltage from a lower value at the input to a higher value at the output. Figure 2.13 shows the circuit schematic of the step-up DC/DC converter to be implemented in the system under study. It is clear by analyzing the figure that the converter is formed by six external components: an inductor, two electronic switches, two diodes, and a capacitor [21].
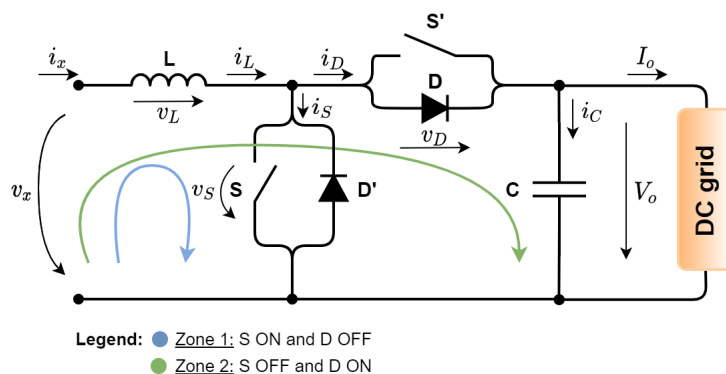
Figure 2.13: Diagram of the boost converter (adapted from [21]).

In steady-state operation and in Continuous Conduction Mode (CCM), the operation modes of the converter can be described by the following expressions (2.3) to (2.8) [21].

- Operating zone 1:
  - $[n\,T_s;\ n\,T_s\ +\ \delta\,T_s]$: S ON and D OFF

$$\begin{cases} i_S & = & i_L \\ v_S & \cong & 0 \ (if\ v_S \ll v_x\ and\ v_S \ll V_o) \end{cases} \tag{2.3}$$

$$\begin{cases} i_D & = & 0 \\ v_D & \cong & -v_x \ (if\ v_S \cong 0) \end{cases} \tag{2.4}$$

$$v_L = v_x \tag{2.5}$$

- Operating zone 2:
  - $[n\,T_s\ +\ \delta\,T_s;\ (n+1)\,T_s]$: S OFF and D ON

$$\begin{cases} i_S & = & 0 \\ v_S & \cong & V_o \ (if\ v_D \cong 0) \end{cases} \tag{2.6}$$

$$\begin{cases} i_D & = & i_L \\ v_D & \cong & 0 \ (if\ v_D \ll v_x\ and\ v_D \ll V_o) \end{cases} \tag{2.7}$$

$$v_L = v_x - V_o \tag{2.8}$$

In expressions from (2.3) to (2.8), $\ll$ implies at least a relation of the order of 10.

Considering a stationary operation, the average value of the voltage in inductance is zero ($v_{L\,av} = 0$), and it is possible to calculate a relationship between the input and output voltages present in the expression (2.9) [21].

$$\frac{V_o}{v_x} = \frac{1}{1-\delta} \Leftrightarrow v_x = (1-\delta)V_o \tag{2.9}$$

Figure 2.14 shows the most relevant waveforms in the operation of the DC/DC Boost Converter. It is important to emphasize that due to the high-frequency switching of the semiconductor, voltage V_o is not exactly constant, presenting a small ripple ΔV_o, which should be neglect.
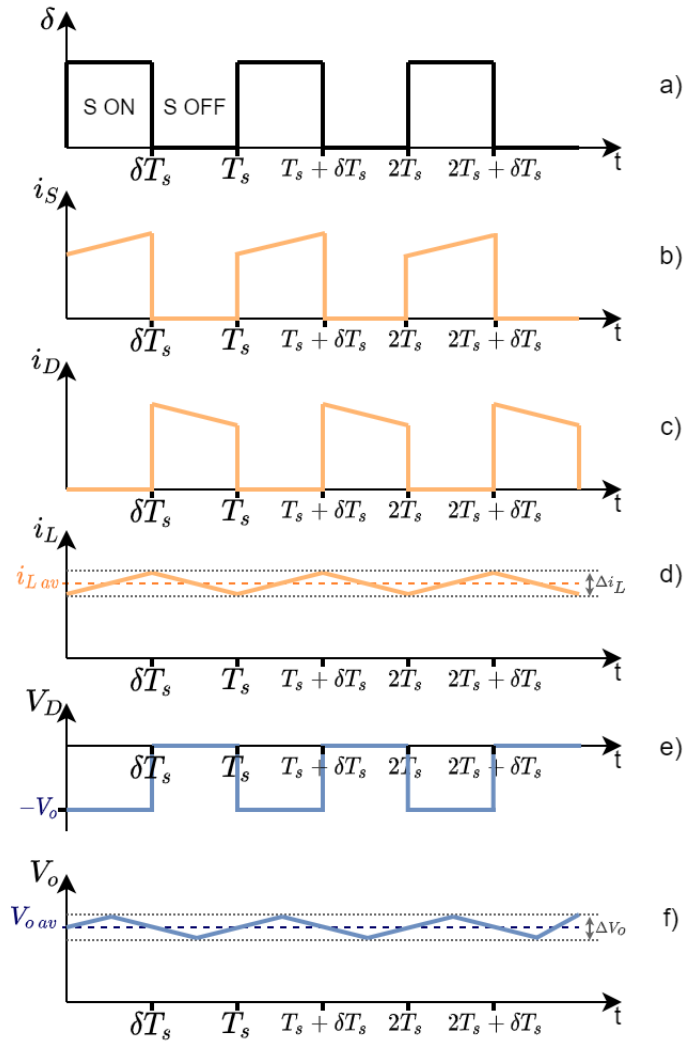
Figure 2.14: DC/DC Boost Converter waveforms of a) semiconductor driving voltage; b) supply current; c) diode current; d) inductor current; e) diode voltage; f) output voltage.

Considering the operating mode of the converter, the voltages and currents present in the converter are almost continuous [17]. However, they present a ripple which is dependent on the filtering components [17]. Based on these characteristics, it is possible to calculate the inductance and the capacitor in the converter [17].

2.4.1 Sizing of L

Expression (2.10) presents the differential equation that describes the progress of the current in L.

$$v_L = L \frac{d\,i_L}{d\,t} \Rightarrow \frac{d\,i_L}{d\,t} = \frac{v_L}{L} \tag{2.10}$$

17

The expression (2.10) can be rewritten by expression (2.11), considering the linearization of the variation of the current.

$$\frac{\Delta i_L}{\Delta t} = \frac{v_L}{L} \tag{2.11}$$

Considering the operation in zone 1 (S ON), the following equities can be assumed: $v_L = v_x$ and $\Delta t = \delta T_s$ reaching expression (2.12), which represents the inductor current ripple. It is important to emphasize that in the computations, the inductance is without losses.

$$\frac{\Delta i_L}{\delta T_s} = \frac{v_x}{L} \Leftrightarrow \Delta i_L = \frac{v_x}{L} \delta T_s \tag{2.12}$$

In this way, by fixing the value of the current ripple and considering the expression (2.9), it is possible to size the filtering inductance, L, through expression (2.13).

$$L = \frac{v_x \delta T_s}{\Delta i_L} = \frac{V_o(1-\delta)\delta T_s}{\Delta i_L} \tag{2.13}$$

It appears by analyzing expression (2.13) that if V_o is constant, L is maximum for $\delta = 1/2$ and is defined by expression (2.14). Since the system under study intends to have a constant V_o voltage, expression (2.14) is used to size L.

$$if\ V_o = const\ \Rightarrow\ L_{max} = \frac{V_o T_s}{4\Delta i_L}\ \ when\ \delta = \frac{1}{2} \tag{2.14}$$

2.4.2 Sizing of C

The expression (2.15) provides the differential equation that describes the progress of the voltage in the capacitor, C.

$$i_C = C\frac{d\,u_C}{d\,t} \Rightarrow \frac{d\,u_C}{d\,t} = \frac{i_C}{C} \tag{2.15}$$

Similarly to the inductor current, the voltage variation of the capacitor is linearized, and expression (2.16) is obtained.

$$\frac{\Delta V_o}{\Delta t} = \frac{i_C}{C} \tag{2.16}$$

Furthermore, ΔV_o can also be described by expression (2.17).

$$\Delta V_o = \frac{\Delta Q}{C} = \frac{1}{wC} \int_{\frac{3\pi}{4}}^{\frac{5\pi}{4}} i_C(wt)\,d\,wt \tag{2.17}$$

Assuming that on the AC grid, both current and voltage are sinusoidal and that the power factor is

18

approximately unitary, the instantaneous power of this same grid is given by expression (2.18).

$$p_{grid}(t) = v_{grid}(t)\, i_{grid}(t) = V_{RMS}\, I_{RMS}[1 + cos(2wt)] \tag{2.18}$$

By neglecting the losses of all the elements of the system under analysis, it becomes possible to achieve expression (2.19).

$$P_{grid} = V_{RMS}I_{RMS} = P_o = V_o I_o \tag{2.19}$$

The power on the DC side is provided by expression (2.20), considering expressions (2.18) and (2.19).

$$p_{dc}(t) = V_o\, i_L(t) = p_{grid} = P_o\,[1 + cos(2wt)] \tag{2.20}$$

The current i_L can be defined by expression (2.21), considering expression (2.20).

$$i_L(t) = I_o\,[1 + cos(2wt)] \tag{2.21}$$

Once the i_L current is set, it is possible to define the i_C current so that later it is possible to establish ΔV_o. Thus, expression (2.22) presents the i_C current definition.

$$i_c(t) = i_L(t) - I_o = I_o\, cos(2wt) \tag{2.22}$$

Consequently, expression (2.17), which defines ΔV_o, can be rewritten as (2.23), using the definition of i_C as in (2.22).

$$\Delta V_o = \frac{I_o}{2\,w\,C}[sin(2wt)]_{\frac{3\pi}{4}}^{\frac{5\pi}{4}} = \frac{I_o}{w\,C} \tag{2.23}$$

Finally, the expression (2.24) is obtained, which allows sizing the C capacitor by setting the value of the V_o voltage ripple, ΔV_o.

$$C = \frac{I_o}{w\,\Delta V_o} = \frac{P_o}{w\,V_o\,\Delta V_o} \tag{2.24}$$

2.5   Constant Power Load

Controlling a DC network presents several challenges, one of the most important being the requirements of the power electronic loads, such as computers or mobile phone chargers, which may be connected to the DC grid [3]. In general, these loads behave as Constant Power Loads (CPL) because, they absorb a constant power, i.e., $dP_{cpl} = 0$ in steady-state [3, 22]. Therefore, it is possible to assume the relation present in expression (2.25) [3].

$$P_{cpl} = V_{o_{cpl}}\, I_{o_{cpl}} = constant \tag{2.25}$$

19

Since dP_{cpl} is equal to zero, it is possible to derive (2.26) and to conclude that, as a result of the power being constant, the load may be represented as a negative incremental resistance, r_i [3].

$$dP_{cpl} = V_{o_{cpl}}\, dI_{o_{cpl}} + I_{o_{cpl}}\, dV_{o_{cpl}} = 0 \Leftrightarrow \frac{dV_{o_{cpl}}}{dI_{o_{cpl}}} = -\frac{V_{o_{cpl}}}{I_{o_{cpl}}} = r_i \qquad (2.26)$$

By analyzing the relation present in expression (2.26), it is possible to verify that if the voltage at the CPL input decreases then the current at its input increases. Therefore, this increase in current causes a further reduction in the system voltage [3]. Then, it is concluded that the presence of CPL can cause a decrease of the equivalent resistance of the system, oscillations in the system voltages and currents, and may also lead to voltage collapse [22].

Figure 2.15 shows the characteristic I-V curve of a CPL. By analyzing it, it is possible to verify that the current is inversely proportional to the voltage, as indicated in expression (2.26).
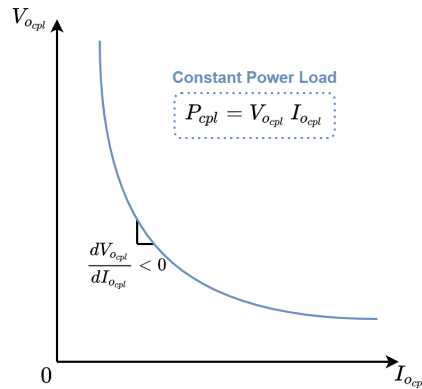
Figure 2.15: Typical Constant Power Load V-I characteristics (adapted from [22]).

A CPL load can have several topologies [22]. In this dissertation, to simplify the analysis without loosing the main control challenges, the CPL consists of a buck converter with an input filter and its control system (explained in detail in chapter 3), as shown in figure 2.16.
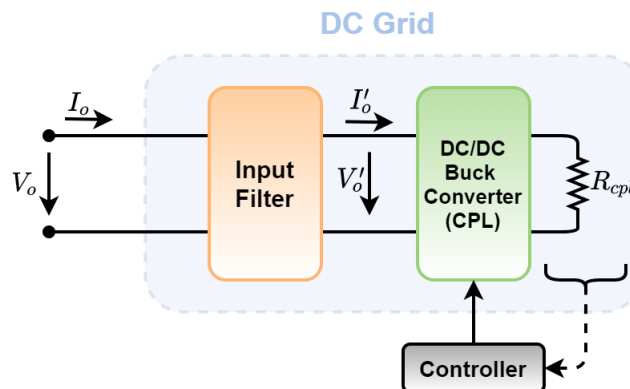
Figure 2.16: DC grid and Constant Power Load configurations.

2.5.1 Step-Down Converter

Step down converters, also known as buck converters, are used whenever it is necessary to reduce a given DC voltage to a lower value [23]. The fundamental topology of a step-down converter can be implemented by the circuit present in figure 2.17, which contains an LC filter, a diode, D_{cpl}, and a switching semiconductor, S_{cpl} [24].
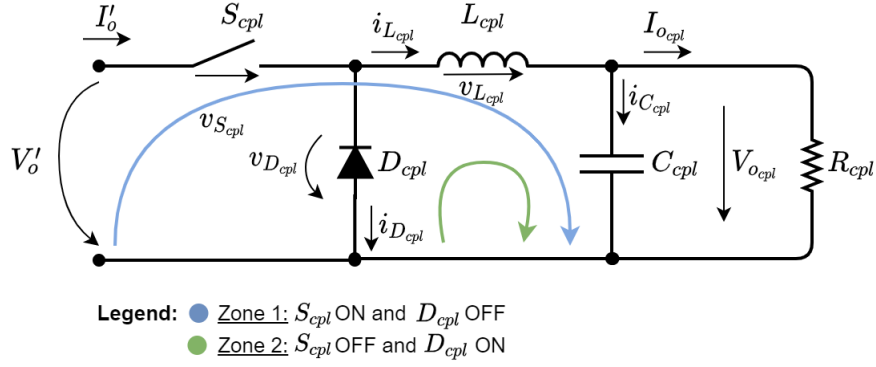
Figure 2.17: Diagram of the buck converter (adapted from [24]).

Expressions (2.27) to (2.32) describe the operation of the buck converter in CCM operating mode in steady state [25].

• Operating zone 1:

 - $[n\,T_s;\ n\,T_s + \delta\,T_s]$: S_{cpl} ON and D_{cpl} OFF

$$\begin{cases} I_o' & = & i_{L_{cpl}} \\ v_{S_{cpl}} & \cong & 0 \ (if\ v_{S_{cpl}} \ll V_o'\ and\ v_{S_{cpl}} \ll V_{o_{cpl}}) \end{cases} \qquad (2.27)$$

$$\begin{cases} i_{D_{cpl}} & = & 0 \\ v_{D_{cpl}} & \cong & V_o' \ (if\ v_{S_{cpl}} \cong 0) \end{cases} \qquad (2.28)$$

$$v_{L_{cpl}} = V_o' - V_{o_{cpl}} \qquad (2.29)$$

• Operating zone 2:

 - $[n\,T_s + \delta\,T_s;\ (n+1)\,T_s]$: S_{cpl} OFF and D_{cpl} ON

$$\begin{cases} I_o' & = & 0 \\ v_{S_{cpl}} & \cong & V_o' \ (if\ v_{D_{cpl}} \cong 0) \end{cases} \qquad (2.30)$$

$$\begin{cases} i_{D_{cpl}} & = & i_{L_{cpl}} \\ v_{D_{cpl}} & \cong & 0 \ (if\ v_{D_{cpl}} \ll V_o'\ and\ v_{D_{cpl}} \ll V_{o_{cpl}}) \end{cases} \qquad (2.31)$$

$$v_{L_{cpl}} = -V_{o_{cpl}} \qquad (2.32)$$

In expressions from (2.27) to (2.32), $\ll$ implies at least a relation of the order of 10.

Considering the operation in the steady-state, both the average value of the capacitor current and the average value of the current in the inductor are null. Therefore, it is possible to assume the relation between V_o' and $V_{o_{cpl}}$ stated in expression (2.33).

$$\frac{V_{o_{cpl}}}{V_o'} = \delta \Leftrightarrow V_{o_{cpl}} = V_o' \delta \tag{2.33}$$

Figure 2.18 shows the most relevant waveforms of the step-down converter. However, as in the boost converter, the voltage has a small ripple, $\Delta V_{o_{cpl}}$ (which should be neglected), due to the high-frequency switching.
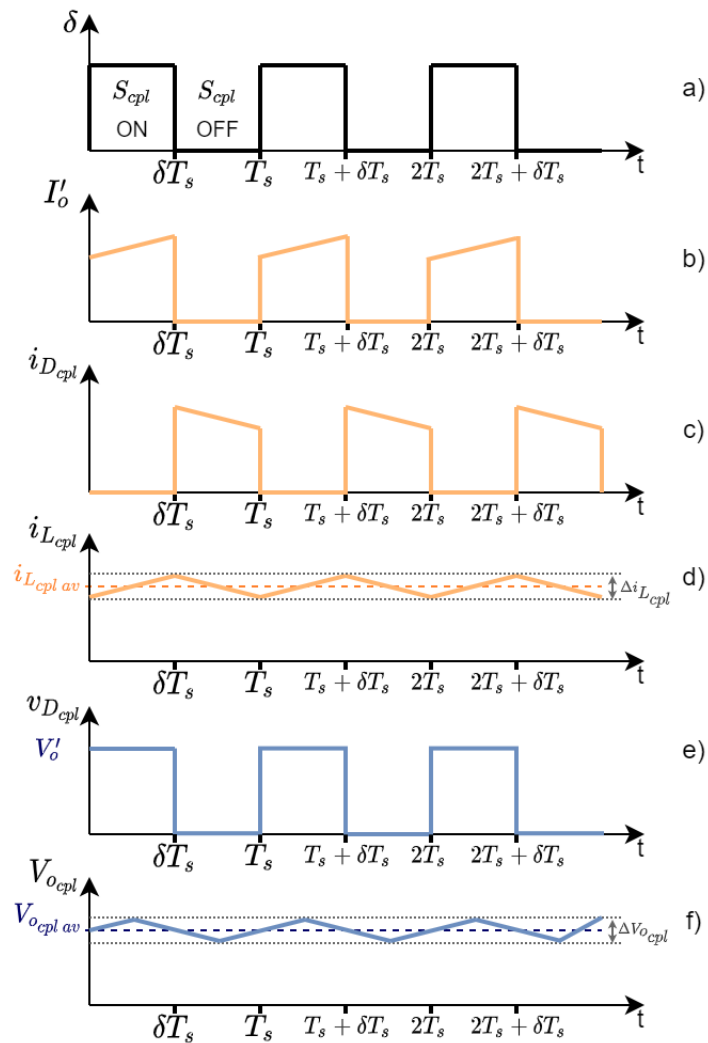
Figure 2.18: DC/DC Buck Converter waveforms of a) semiconductor driving voltage; b) supply current; c) diode current; d) inductor current; e) diode voltage; f) output voltage (adapted from [23]).

22

2.5.2 Sizing of the Filtering Components in the Step Down Converter

As in section 2.4, the components of the buck converter (L_{cpl} and C_{cpl}) are sized. In the case of the inductor, the expressions (2.10) and (2.11) defined in the sizing of the boost converter are still valid. These expressions characterize the progress of the current in the inductor, considering the linearization of this same variable.

Therefore, given the circuit present in figure 2.17, the inductor current ripple, $\Delta i_{L_{cpl}}$, is defined by expression (2.34). This expression assumes operation in zone 1 (S_{cpl} ON and D_{cpl} OFF) and a lossless inductance so, $v_{L_{cpl}} = V'_o - V_{o_{vpl}}$ and $\Delta t = \delta\, T s$ can be assumed.

$$\frac{\Delta i_{L_{cpl}}}{\delta\, T_s} = \frac{V'_o - V_{o_{cpl}}}{L_{cpl}} \Leftrightarrow \Delta i_{L_{cpl}} = \frac{V_{o_{cpl}}\,(1-\delta)\,T_s}{L_{cpl}} \tag{2.34}$$

In this way, by setting the $\Delta i_{L_{cpl}}$ value and considering (2.34), it is possible to obtain (2.35), which presents the L_{cpl} sizing equation.

$$L_{cpl} = \frac{V_{o_{cpl}}\,(1-\delta)\,T_s}{\Delta i_{L_{cpl}}} \tag{2.35}$$

Similar to what was done for the step-up converter, it is possible to simplify the expression (2.35) if we assume that the $V_{o_{cpl}}$ voltage is constant. Therefore, the expression used to size L_{cpl} is given by the expression (2.36).

$$if\ V_{o_{cpl}} = const \ \Rightarrow \ L_{cpl\,max} = \frac{V_{o_{cpl}}\,T_s}{\Delta i_{L_{cpl}}} \ \ when\ \delta = 0 \tag{2.36}$$

The next step is to derive the equation that allows sizing the capacitor. Considering C_{cpl} almost constant and $\Delta V_{o_{cpl}} \ll V_{o_{cpl}}$, it is possible to define the charge variation in the capacitor with expression (2.37).

$$\Delta Q = C_{cpl}\,\Delta V_{o_{cpl}} = \frac{1}{2}\frac{T_s}{2}\frac{\Delta i_{L_{cpl}}}{2} = \frac{T_s\,\Delta i_{L_{cpl}}}{8} \tag{2.37}$$

Considering expression (2.37) and performing some algebraic manipulations, it is possible to size C_{cpl} through expression (2.38). For this, it is necessary to fix the value of the ripple of the $V_{o_{cpl}}$ voltage.

$$C_{cpl} = \frac{T_s\,\Delta i_{L_{cpl}}}{8\,\Delta V_{o_{cpl}}} = \frac{V_{o_{cpl}}\,(1-\delta)\,T_s{}^2}{8L_{cpl}\,\Delta V_{o_{cpl}}} \tag{2.38}$$

Once again, it is possible to simplify the expression (2.38) because it is possible to consider $V_{o_{cpl}}$ constant. Therefore, to size C_{cpl}, we use the expression (2.39).

$$if\ V_{o_{cpl}} = const \ \Rightarrow \ C_{cpl\,max} = \frac{V_{o_{cpl}}\,T_s{}^2}{8\,L_{cpl}\Delta V_{o_{cpl}}} \ \ when\ \delta = 0 \tag{2.39}$$

2.5.3 Input Filter of the Step Down Converter

Real DC power supplies are not capable of guaranteeing precisely constant voltages in their output, respectively, and they also have non-zero output impedances [26]. Therefore, most power converters have a C_f capacitor in parallel with the source to compensate for its internal impedance and thus provide a voltage free of inductive impedance effects [26].

On the other hand, Buck converter consumes current pulses from the supply system [26]. These impulses lead to voltage drops and produce more Electromagnetic Interference (EMI) conducted and radiated to nearby devices and circuits [26]. To avoid the degradation of the quality of the output voltage and to reduce EMI, it is essential to smooth the source current [26]. By including an L_f inductor before the C_f capacitor, the supply current can be softened, thus forming an LC filter [26]. This way, it is possible to guarantee the power quality of the power supply system [26].

However, this input filter can be improved by including an R_f resistance, thus reducing system oscillations [27]. Therefore, R_f can be placed in series or parallel with one of the input filter elements [27]. The possibility chosen is to place R_f in parallel with L_f to have the minimum possible losses and not to create an undesirable ripple in the input voltage. Figure 2.19 shows the inlet filter scheme to be implemented before the CPL.
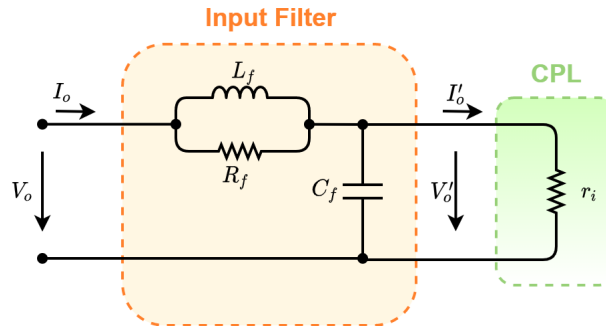
Figure 2.19: Diagram of the input filter (adapted from [26]).

The filters allow attenuating the harmonics originated by the converters [11]. However, it is necessary to size them correctly. Therefore, we begin by defining, through expression (2.40), the system transfer function of figure 2.19 [26].

$$\frac{V_o'(s)}{V_o(s)} = \frac{\frac{1}{C_f L_f}\left(s\frac{L_f}{R_f}+1\right)}{s^2 + s\left(\frac{R_f+r_i}{C_f R_f r_i}\right) + \frac{1}{C_f L_f}} = \frac{\frac{1}{C_f L_f}\left(s\frac{L_f}{R_f}+1\right)}{s^2 + s\frac{\sqrt{\frac{L_f}{C_f}}}{\left(\frac{R_f r_i}{R_f+r_i}\right)}\sqrt{\frac{1}{C_f L_f}} + \frac{1}{C_f L_f}} \tag{2.40}$$

By comparing the denominator of equation (2.40) with the canonical equation of a second-order polynomial, $s^2 + 2\zeta w_c s + w_c^2$, it is possible to deduce that the cut-off angular frequency, w_c, is equal to $\frac{1}{\sqrt{C_f L_f}}$.

Expression (2.41) introduces the characteristic impedance of the LC filter, Z_f [26].

$$Z_f = \sqrt{\frac{L_f}{C_f}} \qquad (2.41)$$

To minimize the influence of the transfer function zero, the real zero $-\frac{R_f}{L_f}$ should be placed to the left and as far as possible from the real part of the conjugated pole, $-\zeta w_c$ [26]. In this way, it is possible the relation present in expression (2.42) between R_f and Z_f.

$$-\frac{R_f}{L_f} < -\zeta w_c \Leftrightarrow R_f > \zeta \frac{L_f}{\sqrt{L_f C_f}} \Leftrightarrow R_f > \zeta Z_f \qquad (2.42)$$

Considering H_f a positive constant greater than or equal to 1, the inequation present in expression (2.42) can be replaced by the equation found in expression (2.43) [26].

$$R_f = H_f \zeta Z_f, \quad H_f \geq 1 \qquad (2.43)$$

It is necessary to apply the relationship of expression (2.44) to ensure the stability of Routh-Hurwitz [26].

$$\frac{R_f + r_i}{C_f R_f r_i} > 0 \Rightarrow \frac{R_f + r_i}{r_i} > 0 \Rightarrow 0 < R_f < -r_i \qquad (2.44)$$

Associating the expressions (2.43) and (2.44) results in expression (2.45).

$$\zeta H_f Z_f < -r_i \Leftrightarrow Z_f < -\frac{r_i}{\zeta H_f} \qquad (2.45)$$

Recalling the canonical form of a second-order polynomial, the definition of Z_f present in expression (2.41), and expression (2.40), which includes the transfer function, it is possible to define R_f through expression (2.46).

$$2\zeta = \frac{Z_f}{\left(\frac{r_f r_i}{r_f + r_i}\right)} \Leftrightarrow R_f = \frac{Z_f r_i}{2\zeta r_i - Z_f} \qquad (2.46)$$

If $\mid 2\zeta r_i \mid$ is at least twice as big as Z_f, it is possible to simplify expression (2.46) by expression (2.47).

$$R_f \approx \frac{Z_f}{2\zeta}, \qquad Z_f \ll \mid 2\zeta r_i \mid \qquad (2.47)$$

By equating expressions (2.43) and (2.46), we obtain expression (2.48), which defines Z_f.

$$\frac{Z_f r_i}{2\zeta r_i - Z_f} = H_f \zeta Z_f \Leftrightarrow Z_f = \frac{r_i \left(2 H_f \zeta^2 - 1\right)}{H_f \zeta} \qquad (2.48)$$

Z_f stands for the characteristic impedance of the LC filter, so it presents a value greater than zero. However, r_i is an incremental negative resistance. Consequently, to guarantee that Z_f is positive, it is

necessary to ensure that the relationships present in the expression (2.49) are fulfilled.

$$1 \leq H_f \leq \frac{1}{2\zeta^2} \tag{2.49}$$

Assuming that H_f is equal to $\frac{1}{3\zeta^2}$, and considering expression (2.48), expression (2.50) defines Z_f.

$$Z_f = -\zeta r_i \tag{2.50}$$

Regarding the cut-off frequency, f_c, it must be at least one decade above the AC grid frequency, f, and one decade below the switching frequency, f_s, as presented in expression (2.51) [11]. On the other hand, the value of the damping factor, ζ, must be between 0.5 and 0.7 [26].

$$f < f_c < f_s \tag{2.51}$$

By setting a value for f_c, ζ, and characterizing the CPL in terms of voltage and power, it is possible to size the input filter elements using expression (2.52).

$$\begin{cases} \begin{array}{rcl} R_f & \approx & Z_f/2\zeta \\ L_f & \approx & Z_f/w_c \\ C_f & \approx & 1/Z_f w_c \\ \\ where: & & \\ Z_f & = & -\zeta r_i \\ r_i & = & -V^2_{o_{cpl}}/P_{cpl} \\ f_c & \Rightarrow & f < f_c < f_s \\ \zeta & \Rightarrow & 0.5 < \zeta < 0.7 \end{array} \end{cases} \tag{2.52}$$

3

Control System Design

Contents

For the system to work duly, it must be ensured that it is suitably controlled. Therefore, it is required to include a control system in the project under development.

The classical linear control systems are based on linearized averaged models of the system and are valid only for small disturbances. As a result, they may fail when they are subject to large deviations from the equilibrium point. Therefore, the control system proposed in this dissertation is non-linear, and it is generically represented by the scheme presented in figure 3.1.
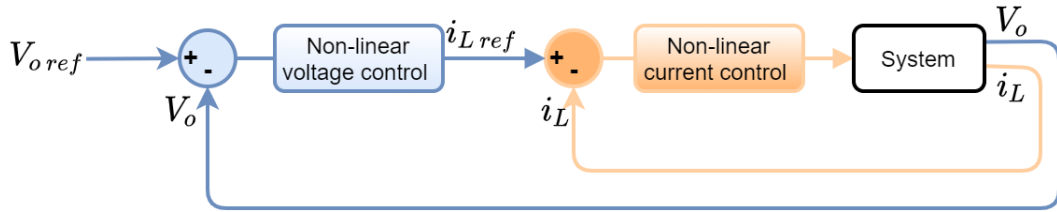
Figure 3.1: Layout of the control system to be implemented.

The proposed solution uses two loops and includes two controllers, one for the voltage and one for the current. The voltage controller, which corresponds to the outer loop, aims to ensure that the V_o voltage follows the reference voltage, $V_{o\,ref}$, and through backstepping theory sets the reference for the i_L current, $I_{L\,ref}$. On the other hand, the inner loop refers to the current controller and aims to ensure that the i_L current follows its reference, $I_{L\,ref}$, based on Sliding Mode Controller.

3.1 Theoretical Fundamentals

Before sizing the controllers, it is necessary to be aware of the theoretical concepts on which the selected methods are based. The following are the theoretical principles of Lyapunov's second method, backstepping theory and sliding mode control.

3.1.1 Stability and Lyapunov's Second Method

When it is intended to design a controller for a non-linear system, it is necessary to guarantee its stability. Following usual practice, stability will always refer to the stability of the null solution, $\mathbf{x} = \mathbf{0}$, of the ordinary differential equation present in expression (3.1) [28]. The equilibrium point of $f(\mathbf{x})$, $\mathbf{x_e}$, corresponds to the origin ($\mathbf{x_e} = \mathbf{0}$) [28].

$$\dot{\mathbf{x}} = f(\mathbf{x}, t), \quad \mathbf{x}(t_0) = \mathbf{x_0} \tag{3.1}$$

Where $\mathbf{x}$ is an n-vector and $f(\mathbf{0}, T) = \mathbf{0}$ [28]. Considering the following definitions, the equilibrium point can be classified as stable, unstable, asymptotically stable, and globally asymptotically stable [29].

- **Stable:** the equilibrium point $\mathbf{x_e}$ of the system (3.1) is stable if, for every real number $\epsilon > 0$, there exists a real number $\delta(\epsilon, t_0) > 0$ such that $\| \mathbf{x_0} - \mathbf{x_e} \| \leq \delta$ implies the expression (3.2) [29]. It is important to note that stability is a local concept in the Lyapunov approach [29].

$$\| \phi(t; \mathbf{x_0}, t_0) - \mathbf{x_e} \| \leq \epsilon \quad \text{for all } t \geq t_0 \tag{3.2}$$

- **Unstable:** when the equilibrium point, $\mathbf{x_e}$, does not meet the conditions to be stable.

- **Asymptotically stable:** the equilibrium point $\mathbf{x_e}$ of the system (3.1) is asymptotically stable if it is stable, and every motion starting sufficiently near $\mathbf{x_e}$ converge to $\mathbf{x_e}$ as $t \rightarrow \infty$ [29]. Mathematically, it means there is some real constant $r(t_0) > 0$, and to every real number $\mu > 0$, it corresponds a real number $T(\mu, \mathbf{x_0}, t_0)$ such that $\| \mathbf{x_0} - \mathbf{x_e} \| \leq r(t_0)$ implies the expression (3.3) [29].

$$\| \phi(t; \mathbf{x_0}, t_0) - \mathbf{x_e} \| \leq \mu \quad \text{for all } t \geq t_0 + T \tag{3.3}$$

- **Globally asymptotically stable:** the equilibrium point $\mathbf{x_e}$ of the system (3.1) is globally asymptotically stable or asymptotically stable in the large if it is stable and every motion converges to $\mathbf{x_e}$ (converges to $\mathbf{x_e}$ uniformly in $\mathbf{x_0}$ for $\| \mathbf{x_0} \| \leq r$, where r is fixed but arbitrarily large) as $t \rightarrow \infty$ [29]. Note that asymptotically and globally asymptotically stability are equivalent if they are uniform in t_0 [29].

Figure 3.2 allows us to graphically distinguish the concepts of stability, instability, and asymptotic stability.
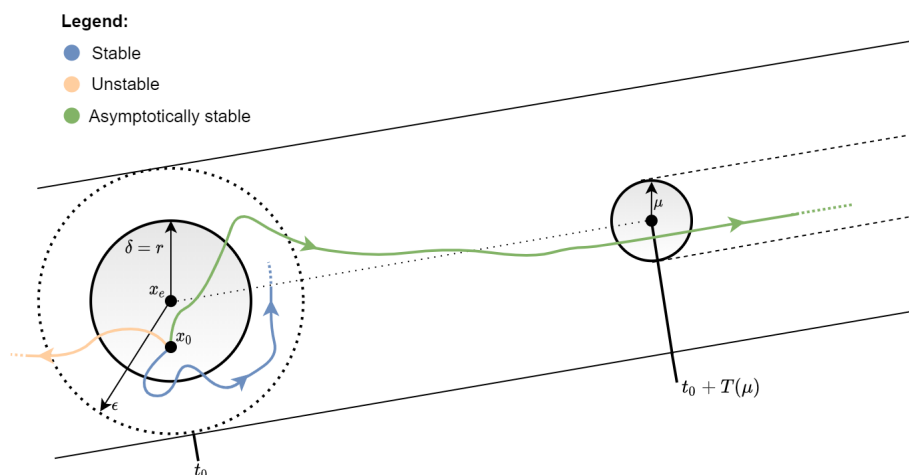
Figure 3.2: Graphical presentation of the concepts of stability, instability, and asymptotic stability (adapted from [29]).

Lyapunov's Second Method (LSM), or also known as the direct method, is a method that allows determining the system stability of the expression (3.1) without solving the equations that form it [28]. This method relies on the following physical reasoning: if the rate of change $dE(x)/dt$ of the energy $E(x)$ of an isolated physical system is negative for every possible state x, except for a single equilibrium state, x_e, then the energy will continually decrease until it finally assumes its minimum value $E(x_e)$ [29]. That is, the intuitive concept of stability presents the following definition: a dissipative system perturbed from its equilibrium state will always return to it [29].

The application of LSM to stability problems consists of defining a Lyapunov function with certain characteristics whose existence implies the type of stability desired [29]. Hence, the system's globally asymptotically stability of the expression (3.1) is ensured by the existence of a scalar function $V(\mathbf{x})$, that must satisfy the following requirements [29]:

1. $V(\mathbf{x}) > 0$ for all $x \neq 0$ and $V(\mathbf{0}) = 0$, i.e., $V(\mathbf{x})$ has to be positive definite.

2. $\dot{V}(\mathbf{x}) < 0$ for all $x \neq 0$ and $\dot{V}(\mathbf{0}) = 0$, i.e., $\dot{V}(\mathbf{x})$ has to be negative definite.

3. $V(\mathbf{x}) \to \infty$ with $\| \mathbf{x} \| \to \infty$, i.e., $V(\mathbf{x})$ has to be "radially unbounded".

3.1.2 Backstepping Controller Design

Backstepping is a control technique developed by Krstic, Kanellakopoulos, and Kokotovic and became an efficient tool in the development of controllers of various non-linear systems [30]. The key idea of this methodology is to break the non-linear system into smaller non-linear systems, i.e., of lower order, and recursively use some states as "virtual controllers" to obtain the laws of intermediate control through Lyapunov's functions [30, 31]. This control technique has several advantages that allow increasing the performance of the system, among them the guarantee of stability and robustness of the system using Lyapunov's functions [30, 32]. To explain the backstepping procedure, a generic non-linear system in the "strict feedback form" is presented in the expression (3.4) [31].

$$
\begin{aligned}
\dot{x}_1 &= f_1(x_1) + g_1(x_1) \cdot x_2 \\
\dot{x}_2 &= f_2(x_1, x_2) + g_2(x_1, x_2) \cdot x_3 \\
&\vdots \\
\dot{x}_n &= f_n(x_1, \cdots, x_n) + g_n(x_1, \cdots, x_n) \cdot u
\end{aligned}
\tag{3.4}
$$

Where $(x_1, x_2, \cdots, x_n) \in \mathbb{R}^n$ are the system states, $u \in \mathbb{R}$ is the control input and $g_i(x_1, x_2, \cdots, x_n) \neq 0$ for $1 < i < n$ [30]. To illustrate simply the backstepping procedure, an example with a system with one state, $n = 1$, is presented below. Therefore, the non-linear system under study is described by (3.5).

$$
\dot{x}_1 = f_1(x_1) + g_1(x_1) \, u
\tag{3.5}
$$

The goal of this problem is to ensure that the system state follows the reference value [32]. In this way, it is possible to define a tracking error variable for x_1 [32]. Expression (3.6) shows the following error variable relative to x_1.

$$z_1 = x_{1\,ref} - x_1 \tag{3.6}$$

The control signal, u, must be set to ensure that the variable $\dot{z}_1$ is asymptotically stable [32]. It is possible to define $\dot{z}_1$ as presented in the expression (3.7), considering the expressions (3.5) and (3.6).

$$\dot{z}_1 = \dot{x}_{1\,ref} - f_1(x_1) - g_1(x_1)\,u \tag{3.7}$$

The following step is to establish a Lyapunov function for the equation explicit in the expression (3.7), presented in the expression (3.8) [30].

$$V_1(z_1) = \frac{1}{2} \cdot z_1^2 \tag{3.8}$$

From the expressions (3.7) and (3.8), it is possible to infer that $\dot{V}_1$ can be described by the equation presented in the expression (3.9) [30].

$$\begin{aligned} \dot{V}_1 &= z_1 \cdot \dot{z}_1 \Leftrightarrow \\ \Leftrightarrow \dot{V}_1 &= z_1 \cdot (\dot{x}_{1\,ref} - f_1(x_1) - g_1(x_1) \cdot u) \end{aligned} \tag{3.9}$$

Recalling the characteristics of a Lyapunov function, V_1 is a positive definite function, and its derivative must be a negative definite function, therefore, obtaining the expression (3.10) [30].

$$\dot{V}_1 = k_1(x_1) < 0. \tag{3.10}$$

Where $k_1(x_1)$ is a function set to ensure that $\dot{V}_1$ is a negative definite function, thus, $k_1(x_1)$ is defined as presented in expression (3.11), where K_1 is a positive gain [30].

$$k_1(x_1) = -K_1 \cdot z_1^2, \qquad K_1 > 0 \tag{3.11}$$

The following step is to establish the control law, as presented in (3.12), according to the (3.9) and (3.10).

$$-K_1 \cdot z_1 = \dot{x}_{1\,ref} - f_1(x_1) - g_1(x_1)\,u \tag{3.12}$$

Placing the expression (3.12) in its explicit form leads to (3.13).

$$u = g_1(x_1)^{-1} \cdot (\dot{x}_{1\,ref} - f_1(x_1) + K_1 \cdot z_1), \qquad K_1 > 0 \tag{3.13}$$

When applying the control law (3.13), the derivative of V_1 will be negative definite, and all criteria to implement Lyapunov's second method are met. Therefore, the objective of the controller is achieved,

and x_1 follows its reference, which is the control law of the expression (3.13).

3.1.3 Sliding Mode Control

Sliding mode control is a non-linear method designed to control linear and non-linear systems, and was proposed in the late 1950s [33, 34]. In the following decades, this method has attracted the interest of the control research community around the world [33].

This approach has several advantages, the major ones being related to its robustness (since the controller dynamics is independent of the system parameters, disturbances, or operating conditions), to the reduction of the system order, and also to the simple implementation in power converters [34, 35].

The following is an example of a second-order system that can be defined by the expressions (3.14) and (3.15).

$$u = a_1 x + a_2 \dot{x} + \ddot{x}, \quad a_1, a_2 - const. \tag{3.14}$$

$$s(x) = cx + \dot{x}, \quad c - const. \tag{3.15}$$

Figure 3.3 shows the state plane $(x, \dot{x})$ of the system under study, and based on its analysis, can be concluded that in the vicinity of the pq segment, the trajectories run in opposite directions, which leads to the appearance of a sliding mode along this line [34]. Additionally, the equation of the switching line, $s(x) = 0$, is presented in the expression (3.16), can be treated as a movement with solutions that depend only on the slope gain c and are invariant to the parameters and disturbances, demonstrating one of the main advantages of the sliding mode [34].

$$cx + \dot{x} = 0 \tag{3.16}$$
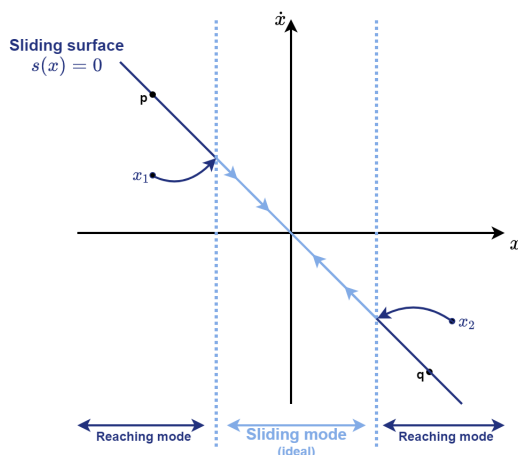
Figure 3.3: Ideal Sliding in a second-order system (adapted from [34, 36]).

Hence, the sliding mode exists if $s(x)$ is equal to 0. However, to remain in this sliding mode the controller must ensure that $\dot{s}(x) = 0$ [35]. Therefore, the sliding mode stability condition, can be written as (3.17) [35].

$$s(x)\dot{s}(x) < 0 \tag{3.17}$$

The control action, u, is designed to ensure the stability condition in (3.17) and can be guaranteed as in (3.18) [34].

$$u = \begin{cases} u^+ & if \quad s(x) > 0 \\ u^- & if \quad s(x) < 0 \end{cases} \tag{3.18}$$

Ideally, it would be desirable that the controlled variable would be exactly equal to the reference value, as presented in figure 3.3. However, this would not be feasible, as this would require that the command signal, u, would commutate between the two structures of the expression (3.18) at an infinitive frequency [34, 35]. As power semiconductors can only switch at a finite frequency [35]. Then, it is necessary to replace the ideal control signal, presented in the expression (3.18), with a real control signal.

Generally, the approach consists of introducing a limit hysteresis $\parallel s \parallel < \Delta$, around the manifold $s(x) = 0$, so that the system trajectories under study are not confined to this manifold but can run arbitrarily inside this new hysteresis band, as shown in figure 3.4 [34].

Therefore, the control signal, u, from the expression (3.18), is replaced by the new control signal from expression (3.19) [35].

$$u = \begin{cases} u^+ & if \quad s(x) > \quad \Delta \\ u^- & if \quad s(x) < \quad -\Delta \end{cases} \tag{3.19}$$
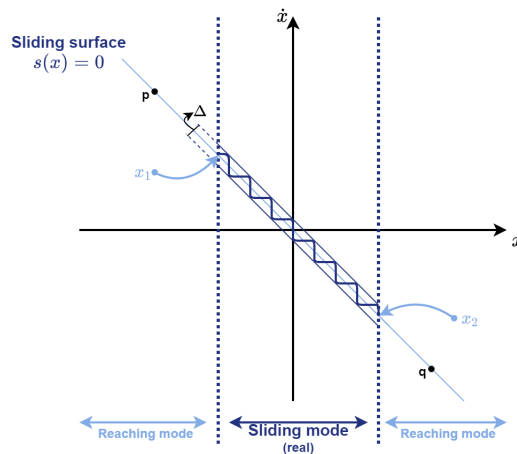
Figure 3.4: Real Sliding in a second-order system (adapted from [34, 36]).

3.2 Control System Design

After the explanation of the theoretical foundations of the methods, the next step consists of sizing the non-linear controllers for the system under study. To do that, it will be necessary to derive the non-linear equations that establish the dynamic behavior of the system [35].

3.2.1 Backstepping Voltage Controller

To design the non-linear voltage controller, the first step consists of inferring the non-linear equation, which defines the variable to control, V_o. For this purpose, Kirchhoff's laws apply to a portion of the system present in figure 2.1. This part of the system contains the boost converter connected to the DC grid and presented in detail in figure 3.5.
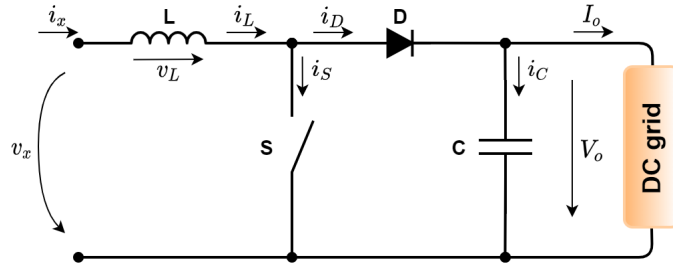
Figure 3.5: Diagram of the boost converter.

By analyzing the figure 3.5, the following expression (3.20) is infered.

$$\dot{V}_o = \frac{i_D - I_o}{C} \tag{3.20}$$

In CCM, the boost converter is known to have two operation zones, as follows [37]:

- 1$^{\text{st}}$ Stage: S ON and D OFF $\Rightarrow i_D = 0$; $i_S = i_L$;

- 2$^{\text{nd}}$ Stage: S OFF and D ON $\Rightarrow i_D = i_L$; $i_S = 0$.

Therefore, when the converter is in the second operating zone, the expression (3.20) can be rewritten as (3.21).

$$\dot{V}_o = \frac{i_L - I_o}{C} \tag{3.21}$$

Since the objective is to guarantee $V_o = V_{oref}$, it is possible to define the V_o voltage error, e_{V_o}, as the difference between the reference signal, V_{oref}, and the measured V_o voltage, as indicated in expression (3.22).

$$e_{V_o} = V_{oref} - V_o \tag{3.22}$$

To ensure e_{V_o} to be zero, the Lyapunov function, V_1, described in the expression (3.23), is proposed.

$$V_1(e_{V_o}) = \frac{1}{2}{e_{V_o}}^2 \tag{3.23}$$

However, to consider the function of expression (3.23) as a Lyapunov's function, the restrictions present in the expression (3.24) must be fulfilled.

$$\begin{cases} V_1(e_{V_o} = 0) & = & 0 \\ V_1(e_{V_o} \neq 0) & > & 0 \\ V_1(|e_{V_o}| \to \infty) & \to & \infty \\ \dot{V}_1(e_{V_o} \neq 0) & < & 0 \end{cases} \tag{3.24}$$

Since the stability condition is $V_1(e_{V_o} \neq 0) \cdot \dot{V}_1(e_{V_o} \neq 0) < 0$, and if V_1 is a positive definite function, it is inferred that the Lyapunov second method global asymptotic stability is described by the expression (3.25).

$$\dot{V}_1 = e_{V_o}\,\dot{e}_{V_o} < 0 \tag{3.25}$$

The expression (3.26) provides a new definition of $\dot{V}_1$ to ensure the condition indicated in the expression (3.25), where K_v is a chosen positive constant to guarantee stability.

$$\dot{V}_1 = -K_v\,{e_{V_o}}^2, \qquad K_v > 0 \tag{3.26}$$

Relating the expressions (3.23) and (3.26) leads to the expression (3.27).

$$\dot{e}_{V_o} = -K_v\,e_{V_o} \tag{3.27}$$

It is possible to derive a new definition for $\dot{e}_{V_o}$, considering the expressions (3.21) and (3.22), which are presented in the expression (3.28).

$$\dot{e}_{V_o} = \dot{V}_{o\,ref} - \dot{V}_o \quad \Leftrightarrow$$
$$\Leftrightarrow \quad \dot{e}_{V_o} = \dot{V}_{o\,ref} - \frac{i_L - I_o}{C} \tag{3.28}$$

Finally, it is possible to derive the law of intermediate control. To this end, $i_{L\,ref}$ replaces i_L, and the definitions of $\dot{e}_{V_o}$, present in the expressions (3.27) and (3.28), are made equal, resulting in (3.29).

$$i_{L\,ref} = C\left(\dot{V}_{o\,ref} + K_v\,e_{V_o}\right) + I_o \tag{3.29}$$

However, $V_{o\,ref}$ is the DC grid reference voltage and is constant, so its derivative is zero. Hence, the

expression (3.29) can be simplified by the expression (3.28).

$$i_{L\,ref} = C\,K_v\,e_{V_o} + I_o \tag{3.30}$$

3.2.1.A   Controller with Integral Action

The intermediate control law defined in the expression (3.30) allows i_L to follow its reference, although it cannot guarantee a zero static error. To guarantee steady state error, it is necessary to increase the complexity of the controller by adding an integral component to it. A new Lyapunov function is defined in (3.31), where K_I is a chosen positive constant.

$$V_2(e_{V_o}) = \frac{1}{2}e_{V_o}{}^2 + K_I\,\frac{e_I{}^2}{2}, \quad K_I > 0 \tag{3.31}$$

Where e_I represents the integral error, as defined in (3.32).

$$e_I = \int_0^t e_{V_o}\,dt = 0 \tag{3.32}$$

From (3.32), the derivative of the error can be calculated as in (3.33).

$$\dot{V}_2 = e_{V_o}\,\dot{e_{V_o}} + K_I\,e_I\,\dot{e_I} \tag{3.33}$$

It is possible to rewrite $\dot{V}_2$ as presented in (3.34), considering (3.32).

$$\dot{V}_2 = e_{V_o}\,\dot{e_{V_o}} + K_I\,e_I\,e_{V_o} \tag{3.34}$$

As in the previous case, the new Lyapunov's function must ensure the restrictions listed in (3.24) and to guarantee the global asymptotic stability. Therefore, it is possible to obtain (3.35).

$$\dot{V}_2 < 0 \Rightarrow \dot{V}_2 = -K_v\,e_{V_o}{}^2, \quad K_v > 0 \tag{3.35}$$

From (3.34) and (3.35), $\dot{e}_{V_o}$ is inferred and presented in (3.36).

$$\dot{e}_{V_o} = -K_v\,e_{V_o} - K_I\,e_I \tag{3.36}$$

After some algebraic manipulations in (3.21), (3.22), and (3.36), it is possible to obtain the new reference value for the current as present in (3.37).

$$i_{L\,ref} = C\,(K_v\,e_{V_o} + K_I\,e_I) + I_o \tag{3.37}$$

From (3.37), it can be seen that the reference value for the current depends on the error of the voltage.

3.2.1.B Synchronization of i_L Current with AC Grid

In the proposed system, the boost converter will have an input current that is not constant, as it would be usual in these converters. In fact, to guarantee the desired operation for the proposed converter, the waveform desired for the i_L current is a rectified sinusoid and synchronous with the AC grid so that the AC grid currents are sinusoidal.

Consequently, the intermediate control law in the expression (3.37) is not sufficient to control the i_L current correctly since it does not provide the desired waveform. The proposed solution consists of multiplying the reference value obtained in (3.37) by a rectified sinusoid, with maximum unitary amplitude and synchronous with the AC network. Mathematically, this rectified sinusoid, Y, can be reached by dividing the AC grid voltage, v_{grid}, by its maximum amplitude, V_M, and then applying the module to it, as described in expression 3.38.

$$Y = \left| \frac{v_{grid}}{V_M} \right| = \left| \frac{v_{grid}}{\sqrt{2}\, v_{grid}(wt)} \right| \tag{3.38}$$

Figure 3.6 presents the block diagram of the Backstepping Voltage Controller to be used for simulation purposes. From this diagram, it is possible to differentiate the variables that are measured, those that are sized, and those that are chosen. Additionally, the proposed controller also includes a limiter, which aims to limit the reference value to avoid it reaching too high values that could damage the system elements. Note that the RMS block, present in figure 3.6, shows in the output the Root Mean Square (RMS) value of the input variable. In this case, the RMS voltage of the AC grid is present in the output.
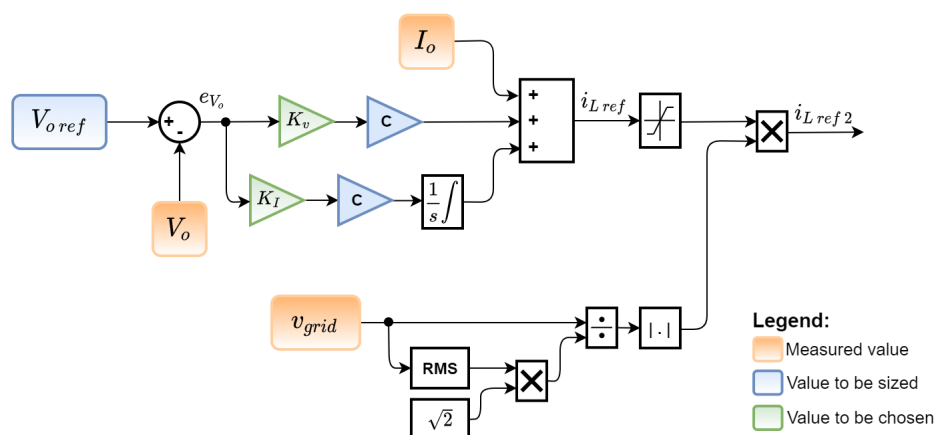

Figure 3.6: Block diagram of the Backsteeping Voltage Controller.

3.2.2 Sliding Mode Current Controller

Once the non-linear voltage controller has been configured, the next and last step in the control system development consists of designing the non-linear current controller. Therefore, the operation of the boost converter present in figure 3.5 is first analyzed, being possible to determine the voltage at the terminals of the inductance from (3.39), (3.40), and (3.41).

$$\gamma = \begin{cases} 1 & if \quad S \ is \ ON \\ 0 & if \quad S \ is \ OFF \end{cases} \tag{3.39}$$

$$\text{if } \gamma = 1 \ \text{ then, } \ v_L = v_x \tag{3.40}$$

$$\text{if } \gamma = 0 \ \text{ then, } \ v_L = v_x - V_o \tag{3.41}$$

Being a boost converter, it is necessary to ensure $V_o > v_x$. Considering this condition and reminding that v_L is defined by $v_L = L\frac{d\,i_L}{dt}$, the expressions (3.42) and (3.43) replace the expressions (3.40) and (3.41), respectively.

$$\text{if } \gamma = 1 \ \text{ then, } \ v_L = v_x \ \Rightarrow \ \frac{d\,i_L}{dt} > 0, \quad V_o > v_x \tag{3.42}$$

$$\text{if } \gamma = 0 \ \text{ then, } \ v_L = v_x - V_o \ \Rightarrow \ \frac{d\,i_L}{dt} < 0, \quad V_o > v_x \tag{3.43}$$

In this case, the goal of the controller is to guarantee $i_L = i_{L\,ref}$, so the i_L current error, e_{i_L}, can be defined as the difference between the reference value, $i_{L\,ref}$, and the measured i_L current, as shown in (3.44).

$$e_{i_L} = i_{L\,ref} - i_L \tag{3.44}$$

To design the sliding mode controller, a linear surface variable in time, $s(x)$, must be defined. Considering the objective of this controller, $s(x)$ is defined as presented in (3.45).

$$s(i_L) = i_{L\,ref} - i_L = e_{i_L} \tag{3.45}$$

To ensure stability, the function $s(x)$, defined in (3.45), must guarantee the sliding mode stability condition, $s(x)\,\dot{s}(x) < 0$. Therefore, it is possible to infer the relations presented in (3.46) and (3.47).

$$\text{if } e_{i_L} > 0 \ \text{ then, } \ \frac{d\,e_{i_L}}{dt} < 0 \ \Rightarrow \ \frac{d\,i_L}{dt} > \frac{d\,i_{L\,ref}}{dt} \tag{3.46}$$

$$\text{if } e_{i_L} < 0 \ \text{ then, } \ \frac{d\,e_{i_L}}{dt} > 0 \ \Rightarrow \ \frac{d\,i_L}{dt} < \frac{d\,i_{L\,ref}}{dt} \tag{3.47}$$

To ensure that the error is within a boundary layer, $-\Delta/2 < e_{i_L} < \Delta/2$, it can be written (3.48) and

(3.49).

$$\text{if } e_{i_L} > +\frac{\Delta}{2} \Rightarrow i_L < i_{L\,ref} \quad \text{then,} \quad i_L \nearrow \quad \text{and} \quad \frac{d\,i_L}{dt} > \frac{d\,i_{L\,ref}}{dt} \tag{3.48}$$

$$\text{if } e_{i_L} < +\frac{\Delta}{2} \Rightarrow i_L > i_{L\,ref} \quad \text{then,} \quad i_L \searrow \quad \text{and} \quad \frac{d\,i_L}{dt} < \frac{d\,i_{L\,ref}}{dt} \tag{3.49}$$

Considering (3.42) and (3.43) and relating them to (3.48) and (3.49), it is possible to define a control law, as in (3.50) and (3.51).

$$\text{if } e_{i_L} > +\frac{\Delta}{2} \Rightarrow i_L \nearrow \quad \text{then,} \quad \frac{d\,i_L}{dt} > 0 \Rightarrow S\ ON(\gamma = 1) \tag{3.50}$$

$$\text{if } e_{i_L} < -\frac{\Delta}{2} \Rightarrow i_L \searrow \quad \text{then,} \quad \frac{d\,i_L}{dt} < 0 \Rightarrow S\ OFF(\gamma = 0) \tag{3.51}$$

Summarizing, when the measured i_L current is smaller than its reference, $i_{L\,ref}$, the switch is turned on to increase the i_L value. Otherwise, the switch is turned off to lower the current i_L value. This can be described mathematically by (3.52).

$$\gamma = \begin{cases} 1 & if \quad e_{i_L} > +\Delta/2 \\ 0 & if \quad e_{i_L} < -\Delta/2 \end{cases} \tag{3.52}$$

In the proposed solution, the implementation of (3.52) consists of controlling the semiconductor S through the signal coming from a hysteresis comparator. This comparator aims to detect if the i_L current error, e_{i_L}, is inside or outside the defined hysteresis, $-\Delta/2 < e_{i_L} < \Delta/2$. Figure 3.7 shows the block diagram of the Sliding Mode Current Controller used for simulation purposes, where the hysteresis comparator is included.
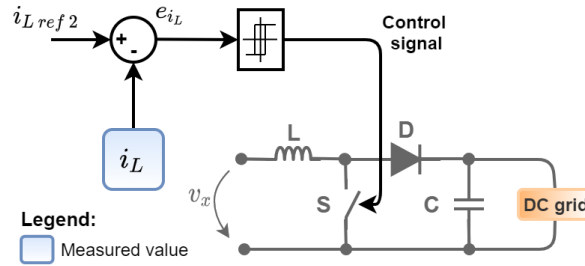
Figure 3.7: Block diagram of the Sliding Mode Current Controller.

3.3 Constant Power Load Control System

To control the CPL the choice is to include a non-linear control system to control the voltage of the CPL and the current in the L_{cpl} inductor. As in the previous system, the control laws follow Lyapunov's stability theory.

The control laws for this new system are derived in a way similar to the one previously used for the

core system. So, the explanation for this new case will be more succinct, presenting only the main steps. As before, we assume that electrical and semi-conductor devices are ideal. Therefore, we begin by defining the non-linear equation of the CPL voltage, as in (3.53), considering the diagram in figure 2.17, which includes the CPL scheme.

$$\dot{V}_{o_{cpl}} = \frac{i_{L_{cpl}} - I_{o_{cpl}}}{C_{cpl}} \tag{3.53}$$

In this case, the goal is to guarantee $V_{o_{cpl}} = V_{o_{cpl\,ref}}$. Therefore, a new control error is defined in (3.54).

$$e_{V_{o_{cpl}}} = V_{o_{cpl\,ref}} - V_{o_{cpl}} \tag{3.54}$$

It is proposed the function Lyapunov, V_3, (3.55), to ensure that $e_{V_{o_{cpl}}}$ is zero and to have a null stationary error. This function presents an integral component through the inclusion of integral error, $e_{I_{cpl}}$, as in (3.56).

$$V_3(e_{V_{o_{cpl}}}) = K_I \frac{e_{I_{cpl}}{}^2}{2} + \frac{e_{V_{o_{cpl}}}{}^2}{2}, \quad K_I > 0 \tag{3.55}$$

$$e_{I_{cpl}} = \int_0^t e_{V_{o_{cpl}}}\, dt = 0 \tag{3.56}$$

The next step is to ensure the stability condition $\left(V_3\left(e_{V_{o_{cpl}}} \neq 0\right)\dot{V}_3\left(e_{V_{o_{cpl}}} \neq 0\right) < 0\right)$. Since V_3 is a positive defined function, then $\dot{V}_3$ must be smaller than zero. In this way, it is possible to define $\dot{e}_{V_{o_{cpl}}}$ from $e_{V_{o_{cpl}}}$ and $e_{I_{cpl}}$, as in (3.57).

$$\dot{V}_3 < 0 \Leftrightarrow \dot{V}_3 = K_I e_{I_{cpl}} e_{V_{o_{cpl}}} + e_{V_{o_{cpl}}} \dot{V}_{o_{cpl}} \rightarrow \dot{e}_{V_{o_{cpl}}} = -K_v e_{V_{o_{cpl}}} - K_I e_{I_{cpl}} \tag{3.57}$$

In this way, it is now feasible to derive the control law that defines the reference of the $i_{L_{cpl}}$ current, in (3.58). For this purpose, equations (3.53), (3.54), and (3.57) have been considered.

$$i_{L_{cpl\,ref}} = C_{cpl}\left(K_v \dot{e}_{V_{o_{cpl}}} + K_I e_{I_{cpl}} + \dot{e}_{V_{o_{cpl}}}\right) + I_{o_{cpl}} \tag{3.58}$$

At this moment, the voltage controller is set, and to have the complete control system, it is necessary to establish the non-linear current controller. This controller is based on the sliding mode control theory. The design of the controller is analogous to the one used in the proposed system. For that reason, only the fundamental steps of the design are presented.

The error of the variable to be controlled is in (3.59) and presents $e_{i_{L_{cpl}}}$, which represents the control error of the $i_{L_{cpl}}$ current.

$$e_{i_{L_{cpl}}} = i_{L_{cpl\,ref}} - i_{L_{cpl}} \tag{3.59}$$

Considering the objective of this controller, the linear surface variable in time, $s(x)$, is defined as presented in (3.60).

$$s(i_{L_{cpl}}) = i_{L_{cpl\,ref}} - i_{L_{cpl}} = e_{i_{L_{cpl}}} \tag{3.60}$$

It is necessary to ensure the condition of sliding mode convergence, $s(x)\,\dot{s}(x) < 0$. When the buck converter switch (S_{cpl}) is ON, $d\,i_{L_{cpl}}/dt > 0$ because in this situation $V_{L_{cpl}} = V'_o - V_{o_{cpl}} > 0$. When ($S_{cpl}$ OFF) then $d\,i_{L_{cpl}}/dt < 0$, since in this case $V_{L_{cpl}} = -V'_o < 0$. Taking all this into account and following a procedure similar to the one used in section 3.2.2, it is possible to reach (3.61) and (3.62).

$$if\ e_{i_{L_{cpl}}} > +\frac{\Delta}{2} \ \Rightarrow \ i_{L_{cpl}} < i_{L_{cpl\,ref}} \ \Rightarrow \ i_{L_{cpl}} \nearrow \quad then,\ \frac{d\,i_{L_{cpl}}}{dt} > 0 \Rightarrow S_{cpl}\ ON \tag{3.61}$$

$$if\ e_{i_{L_{cpl}}} < -\frac{\Delta}{2} \ \Rightarrow \ i_{L_{cpl}} > i_{L_{cpl\,ref}} \ \Rightarrow \ i_{L_{cpl}} \searrow \quad then,\ \frac{d\,i_{L_{cpl}}}{dt} < 0 \Rightarrow S_{cpl}\ OFF \tag{3.62}$$

It is possible to define the operating mode of the buck converter, as shown in (3.63), considering the relations previously mentioned.

$$\gamma_{cpl} = \begin{cases} 1 & if \ \ e_{i_{L_{cpl}}} > +\Delta/2 \\ 0 & if \ \ e_{i_{L_{cpl}}} < -\Delta/2 \end{cases} \tag{3.63}$$

Figure 3.8 shows the block diagram of the control system to be applied to the CPL, which includes the non-linear voltage and current controller. This is the block diagram to be used in the simulations.
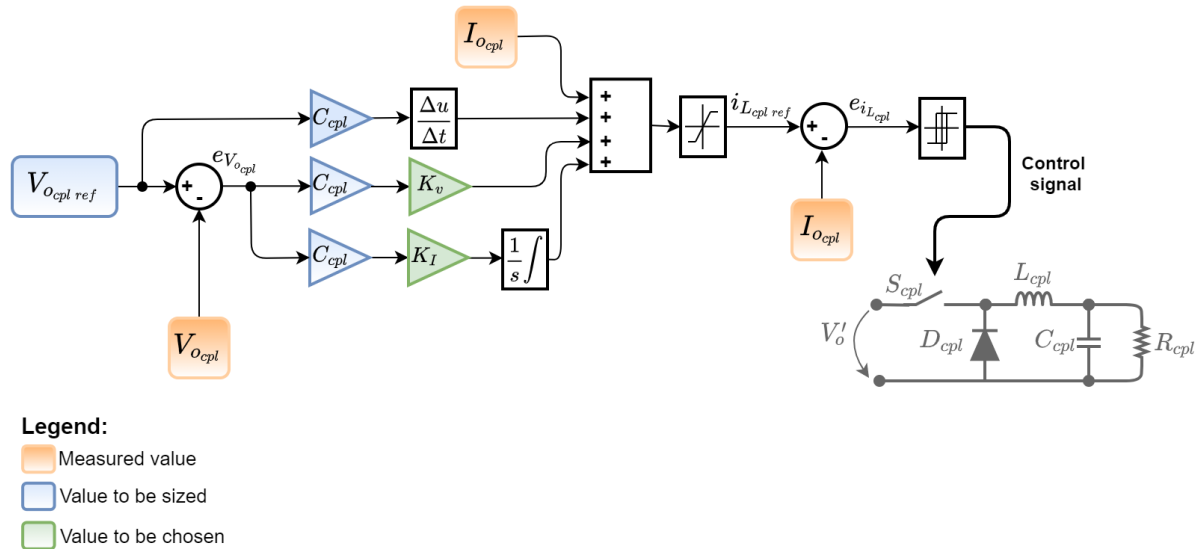
Figure 3.8: Block diagram of the Constant Power Load control system.

4

Simulation Results

Contents

This chapter presents the parameter values and the results obtained in the simulation of different operation scenarios to analyze the system behavior. The cases considered in simulation differ from each other by the operating conditions of the DC grid, and all the simulations were performed using Matlab's Simulink tool.

Figure 4.1 shows the diagram of the system in the simulation, from left to right, it includes the AC grid, followed by the AC/AC matrix converter, and the HFT. Then, connected to the HFT is the AC/DC matrix converter, followed by the boost converter, and in the rightmost part of the system is the DC grid. Besides these elements, the simulation also includes measuring equipment (such as voltmeters and ammeters) and the non-linear control system, represented by the red rectangle, as can be seen in figure 4.1. Appendix B shows all the simulation schemes that make up the system, including the sub-system schemes present in figure 4.1.
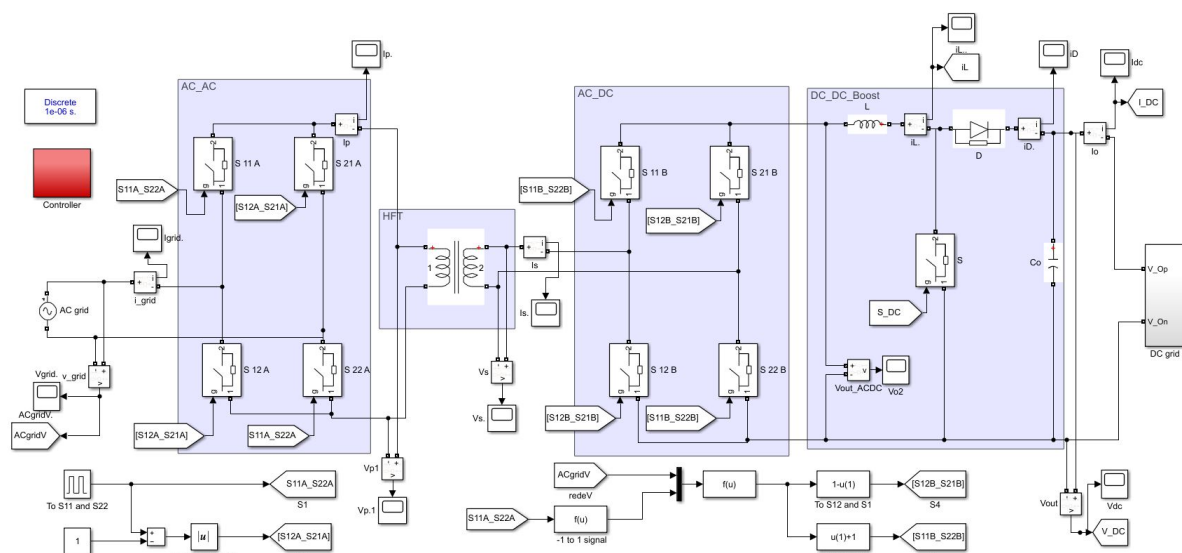
Figure 4.1: Schematic of the simulated system.

4.1 Simulation Parameters

This section presents the parameter values that characterize the proposed system. Table 4.1 shows the parameters of the AC and DC networks as well as the switching frequency value.

Table 4.1: Simulation parameters of the AC and DC grids and the used switching frequency.

AC Grid		DC Grid		
V_{RMS} [V]	f [Hz]	V_{oref} [V]	P_o [kW]	f_s [kHz]
230	50	400	2	50

It is important to stress that the choice of the DC grid voltage reference value, V_{oref} is not arbitrary.

This voltage value is the one that is usually considered for "high voltage" DC grids.

Table 4.2 shows the nominal values of the HFT, while table 4.3 presents the values chosen for the HFT parameters based on the sizing described in Appendix A.

Table 4.2: High Frequency Transformer nominal values.

HFT Nominal Values			
V_p [V]	V_s [V]	P_n [kVA]	f_s [kHz]
230	230	2	50

Table 4.3: High Frequency Transformer parameters.

High-Frequency Transformer					
R_{T1}	R_{T2}	L_{T1}	L_{T2}	R_m	L_m
$0.106\,\Omega$	$0.106\,\Omega$	$1.587\,\mu H$	$1.587\,\mu H$	$5.290\,k\Omega$	$2.846\,H$
0.004 p.u.	0.004 p.u.	0.019 p.u.	0.019 p.u.	200 p.u.	$3.381e^4$ p.u.

Finally, table 4.4 shows the values considered to the boost converter, based on the sizing provided in section 2.4.

**Table 4.4:** Boost converter parameters.

Boost Converter					
V_o [V]	f_s [kHz]	Δi_L	ΔV_o	L [mH]	C [mF]
400	50	$10\%\,i_L$	$1\%\,V_o$	2.3	3.979

4.1.1   Control System Parameters

Regarding the control system described in chapter 3, it is necessary to set the values for K_v and K_I gains so that it is possible to incorporate the control system in the simulation. However, the only restriction imposed on these gains is that they both must be positive constants, according to (3.31) and (3.35).

Several tests are performed, where one of the gains is kept constant, and the other is changed so that it is possible to analyze separately the influence that each one has on the results. Finally, the results are compared, and the best values are used.

To select a reasonable value for the K_v gain, the value of K_I was set to $20 \cdot 10^3$, and the system was simulated with K_v equal to 40, 80, 100, 250, and 500. Figure 4.2 shows the waveform of the voltage in the DC grid, V_o, for the various cases mentioned above. Analyzing figure 4.2, it appears that the results do not change much. However, it is possible to see that the increase in the K_v gain leads to a decrease in the amplitude of oscillations during the transient period.

45
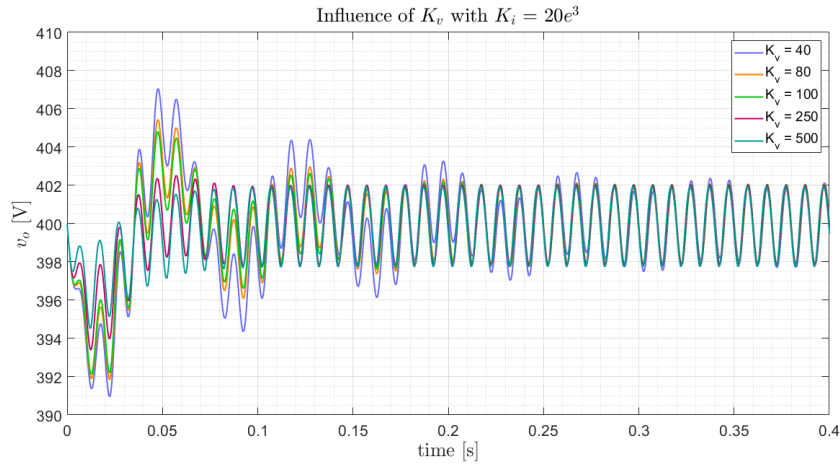
Figure 4.2: Voltage waveform in the DC grid with $K_I = 20 \cdot 10^3$ and $K_v = 40$ (blue), $K_v = 80$ (orange), $K_v = 100$ (green), $K_v = 250$ (pink), and $K_v = 500$ (turquoise).

In the case of the K_I gain, the procedure is analogous to the K_v gain. Therefore, it is considered K_v equal to 40, and the system is simulated for the cases where K_I is equal to $0.5 \cdot 10^3$, 10^3, $10 \cdot 10^3$, $20 \cdot 10^3$, and $50 \cdot 10^3$. Figure 4.3 shows the V_o waveform in the different situations previously referred.
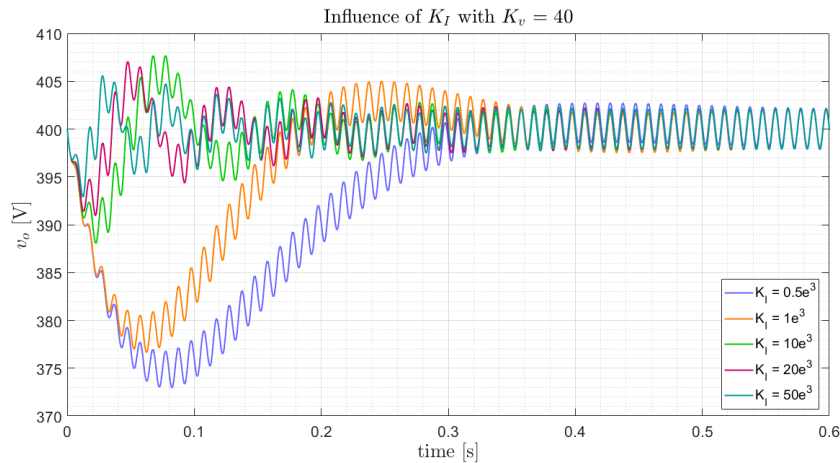

Figure 4.3: Voltage waveform in the DC grid with $K_v = 40$ and $K_I = 0.5 \cdot 10^3$ (blue), $K_I = 10^3$ (orange), $K_I = 10 \cdot 10^3$ (green), $K_I = 20 \cdot 10^3$ (pink), and $K_I = 50 \cdot 10^3$ (turquoise).

It is possible to verify, from figure 4.3, that the K_I gain has a significant impact on the duration of the transient period. It becomes clear that as the K_I gain increases, the transient decreases.

If we only consider the results illustrated in figures 4.2 and 4.3, we can be led to think that the best solution is to have high values for K_v and K_I. However, it is necessary to check if, in the AC network, the waveforms are following the desired ones. Therefore, figures 4.4 and 4.5 present the current waveforms in the AC network for the different cases.
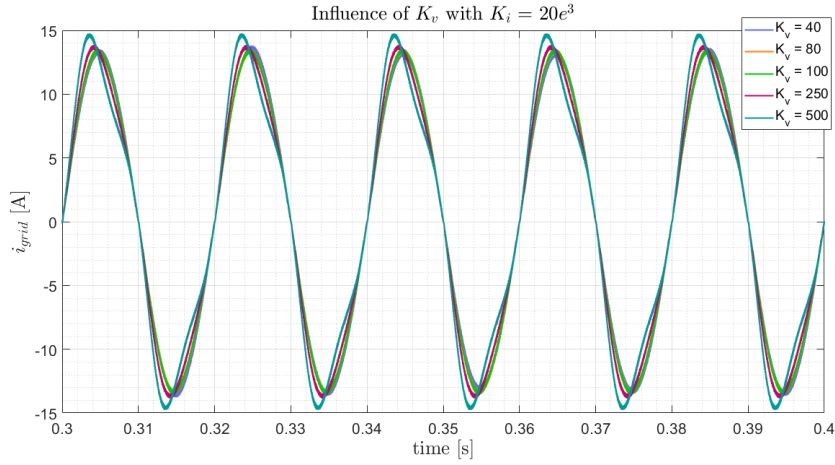
Figure 4.4: Current waveform in the AC grid with $K_I = 20e^3$ and $K_v = 40$ (blue), $K_v = 80$ (orange), $K_v = 100$ (green), $K_v = 250$ (pink), and $K_v = 500$ (turquoise).
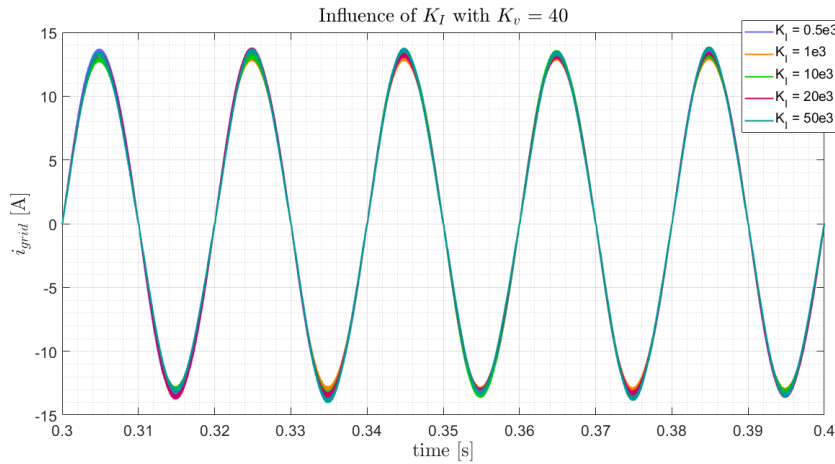
Figure 4.5: Current waveform in the AC grid with $K_v = 40$ and $K_I = 0.5e^3$ (blue), $K_I = 1e^3$ (orange), $K_I = 10e^3$ (green), $K_I = 20e^3$ (pink), and $K_I = 50e^3$ (turquoise).

It is observed in figure 4.5 that the variation of K_I value does not cause changes in the current waveform in the AC network after the transient period. However, it is evident in figure 4.4 that high K_v values lead to distortion of the i_{grid} waveform. For this reason, K_v equals 80, and K_I equals $20e^3$.

4.2   Study Scenarios

This section presents in detail the results obtained in the four scenarios considered. The first case consists of defining the DC network with a resistive load only. The second is similar to the first, although, instead of having only one load, it presents two resistive loads in parallel. In the third situation, the DC grid is composed of a constant power load while, in the fourth scenario, the DC grid is represented

by a current source. Appendix C shows the code of the .m file used to size all the components of the simulated system.

4.2.1 DC Grid with a Single Resistive Load

In this case study, the DC grid is represented only by a resistive load, as shown in figure 4.6, where R_o is equal to $80\,\Omega$.
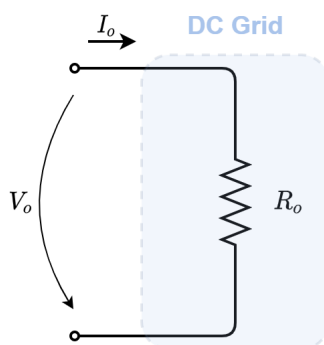
Figure 4.6: DC grid represented only by a resistive load.

The AC grid is defined by an AC voltage source characterized by the parameters presented in table 4.1. Figure 4.7 shows the simulation results of the AC grid in steady-state operation, which include the voltage waveform in blue and the current waveform in orange.
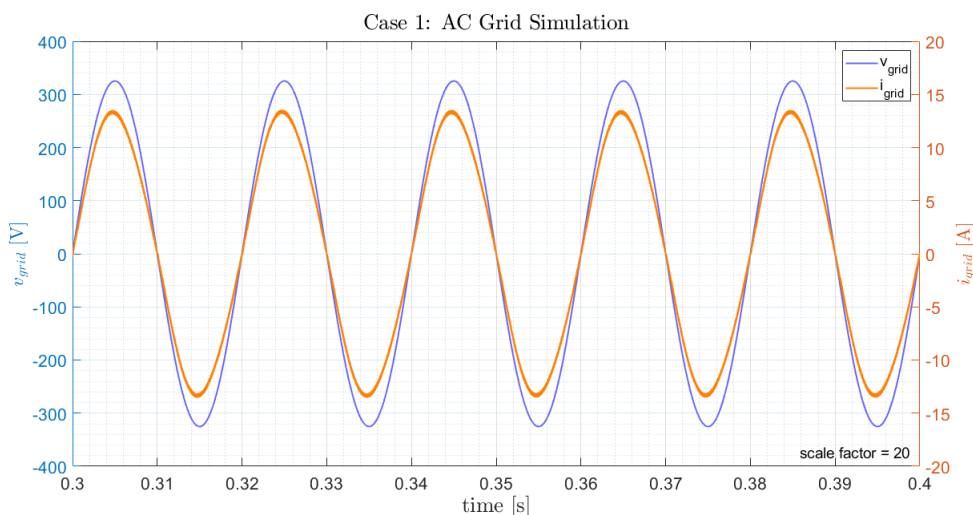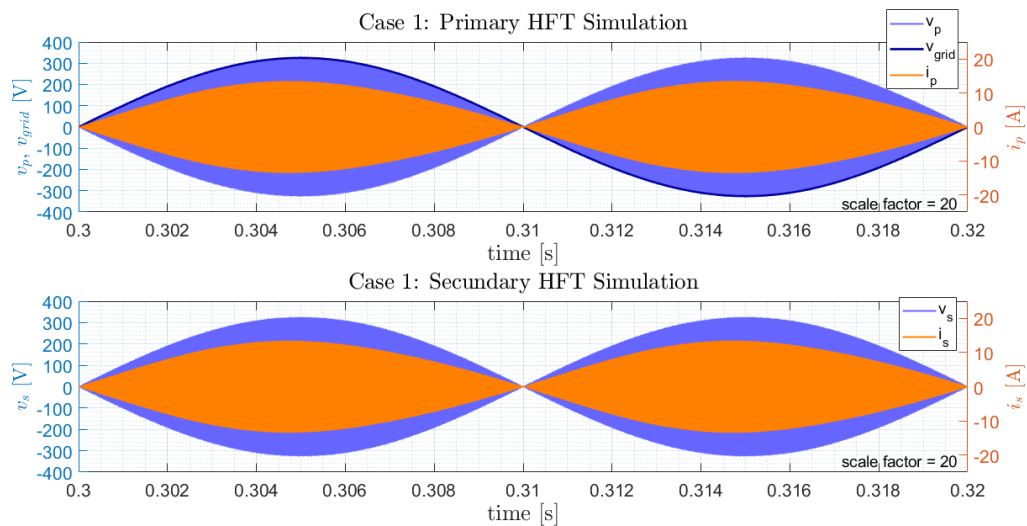

Figure 4.7: AC grid simulation results in case 1: voltage waveform (blue) and current waveform (orange).

It is possible to conclude, by analyzing the figure 4.7, that the AC grid current presents the desired behavior, that is, both voltage and current have a sinusoidal waveform. Furthermore, the voltage and current are in phase, so it is achieved a unitary power factor.

Figure 4.8 presents the simulation results of the High Frequency Transformer. The upper graph shows the current and voltage applied to the primary side of the HFT, while the lower one shows the voltage and current of the secondary.
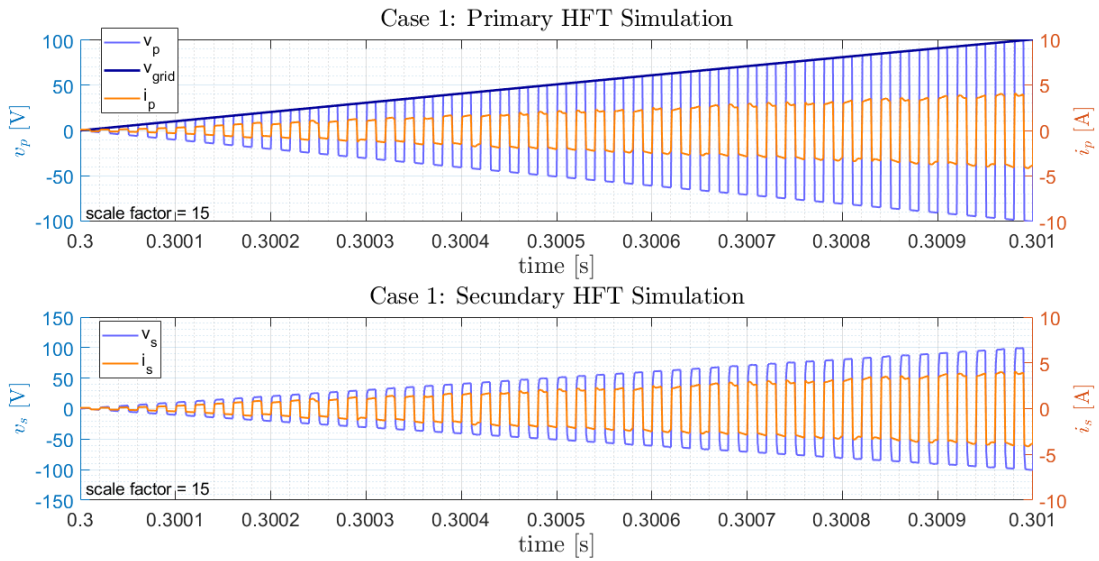

Figure 4.8: HFT simulation results in case 1. Upper graph: primary voltage (light blue) and current (orange) and also AC grid voltage (dark blue). Lower graph: secondary voltage (blue) and current (orange).

The voltage in the HFT input corresponds to the voltage generated by the AC/AC matrix converter. In chapter 2.3.3, the goal of this matrix converter was explained, and by comparing figures 2.11 and 4.8, it is possible to conclude that this goal was achieved. The converter is well controlled because it is possible to transform the AC grid voltage into a voltage with the same amplitude but switched at 50 kHz.

Regarding the secondary of the HFT, both voltage and current are identical to the corresponding variables of the primary. They are similar even in terms of amplitude since the transformation ratio of the HFT is 1:1. Therefore the results are according to those expected.

However, figure 4.8 only allows a general analysis. For a more detailed analysis, figure 4.9 is shown, which contains the same variables as figure 4.8, although it presents a smaller time interval. From this figure, it is already possible to observe the switching at 50 kHz of the different signals under analysis.

Figure 4.9: HFT detail simulation results in case 1. Upper graph: primary voltage (light blue) and current (orange) and also AC grid voltage (dark blue). Lower graph: secondary voltage (blue) and current (orange).

To analyze the operation of the boost converter, the waveform of the inductor current has been simulated. Figure 4.10 shows the waveform of the boost converter inductor current in steady-state operation.
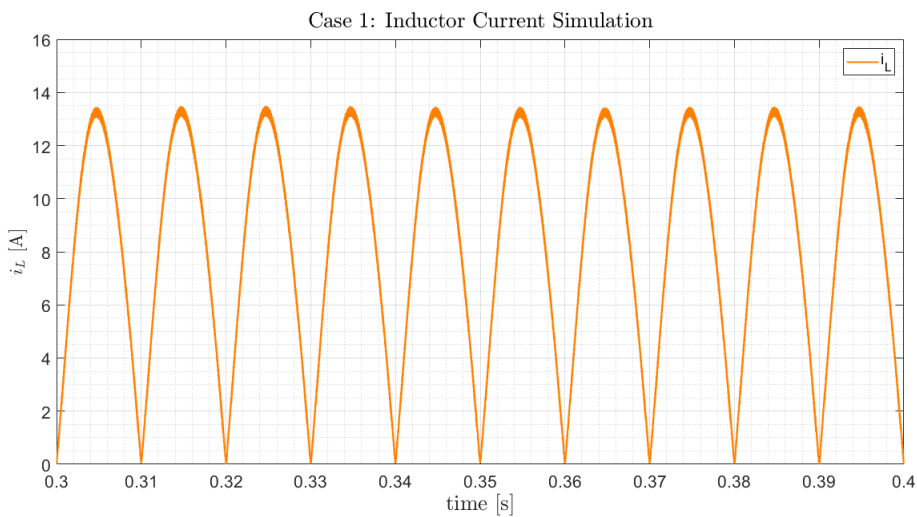
Figure 4.10: Inductor current simulation result in case 1.

As already mentioned in section 3.2.1.B, it is intended to have i_L as a rectified sinusoidal waveform and synchronous with the AC grid. Therefore, and analyzing figure 4.10, it appears that this objective has been achieved. Figure 4.11 shows the i_L control error, so it is possible to prove that the goal was met since the difference between i_L and its reference is never higher than 0.4 A.
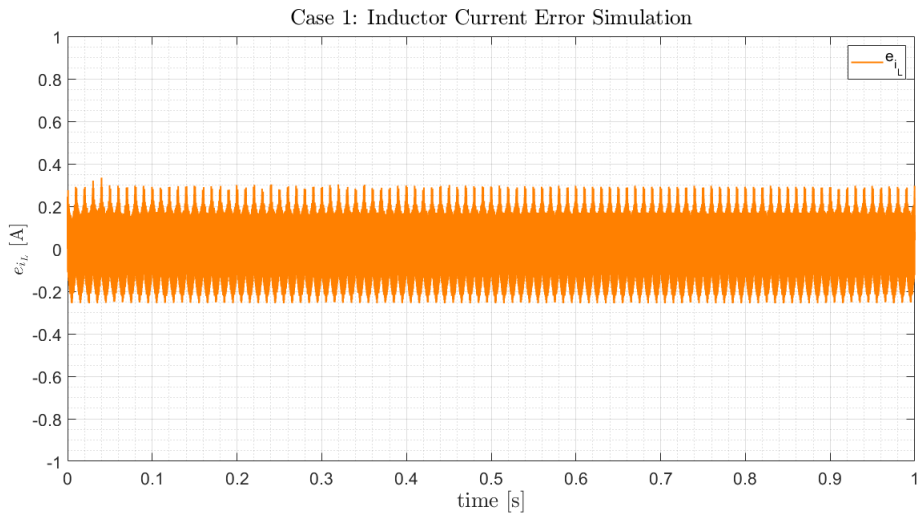
Figure 4.11: Inductor current control error simulation result in case 1.

Figure 4.12 introduces the simulation results for the DC network when it consists of only one resistance. The blue signal represents the voltage V_o in the DC grid, while the orange one represents the current I_o injected in the DC grid.
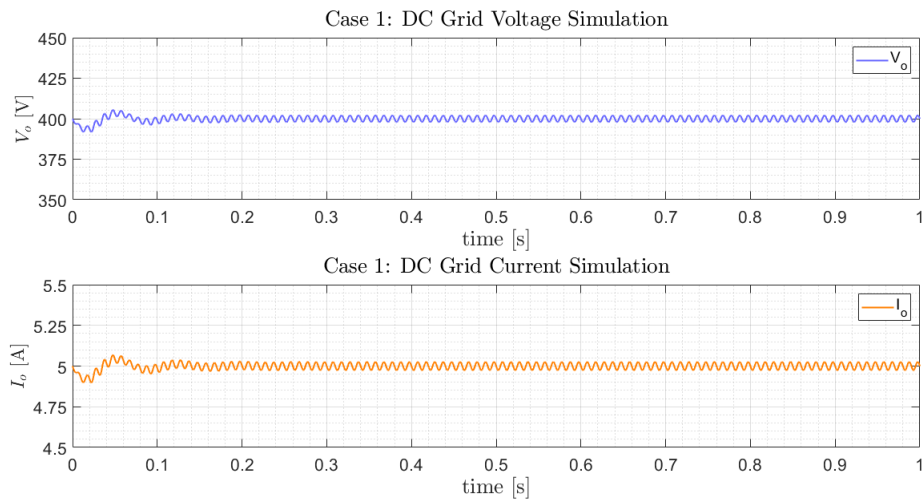
Figure 4.12: DC grid simulation results in case 1: voltage waveform (blue) and current waveform (orange).

Looking at the graphs in figure 4.12, the results are in line with expectations. The V_o voltage is approximately constant and follows its reference value, which is equal to 400 V. Also the I_o current presents an almost constant waveform. To support the previous statements, figure 4.13 shows the variation of the V_o control error throughout the simulation. From this graph, it is evident that the voltage under study follows its reference value.

51
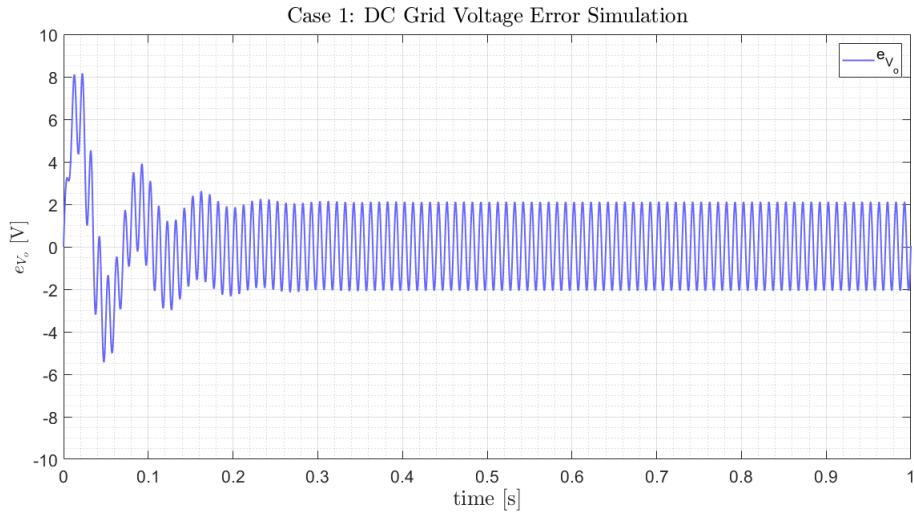
Figure 4.13: DC grid voltage control error simulation result in case 1.

As already mentioned in section 2.4, the voltage of the DC network will never be precisely constant since there will always be a small ripple due to the high-frequency switching. However, it is necessary to verify that this ripple is not higher than the value fixed in the sizing of the boost converter. As indicated in table 4.4, ΔV_o is equal to 1% of V_o, so through figure 4.14, it is ripple has an acceptable values, and the results are as expected.
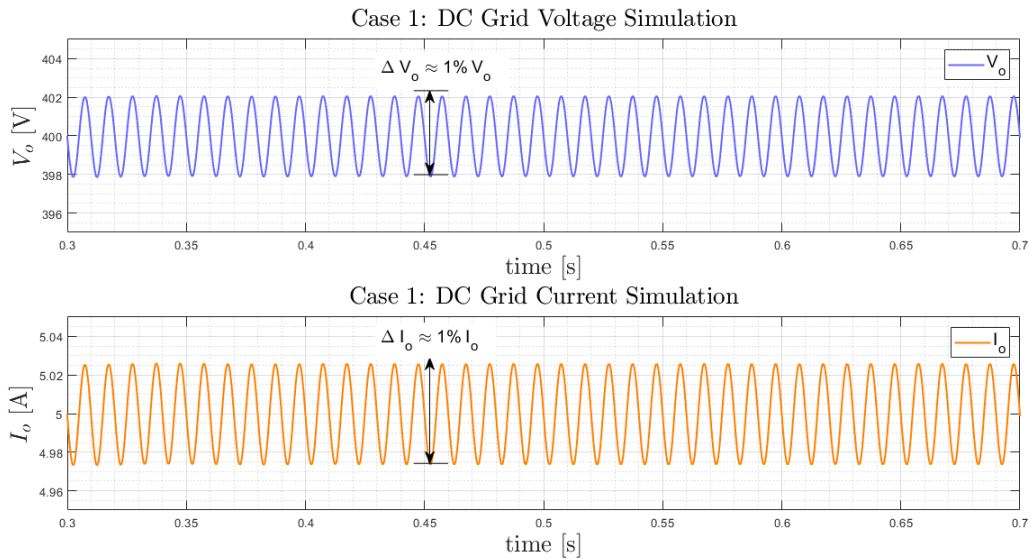
Figure 4.14: Measurement of voltage (blue) and current (orange) ripples of the DC grid in case 1.

52

4.2.2   DC Grid with Two Resistive Loads in Parallel

The second simulated case presents the DC grid characterized by two resistive loads in parallel, as shown in figure 4.15, where R_1 and R_2 are equal to $160 \, \Omega$. The simulation starts only with R_1 load connected, and only at time instant t_1 the load R_2 is connected. In the test run, the time instant t_1 was considered equal to 0.5 s.
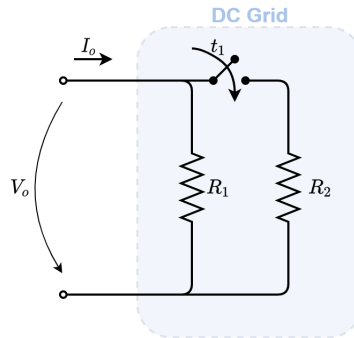
Figure 4.15: DC grid represented by two resistive loads in parallel.

In this simulation, the system up to the instant equal to 0.5 s is the same as the initial case, except for the value of the DC network load. Consequently, it is from this instant that it becomes relevant to observe the results since it is from this moment that the system has two loads in parallel. Figure 4.16 presents the results of the AC network in a time interval that includes the time instant when the second load is connected. The blue graphic represents the voltage waveform, and the orange shows the current waveform.
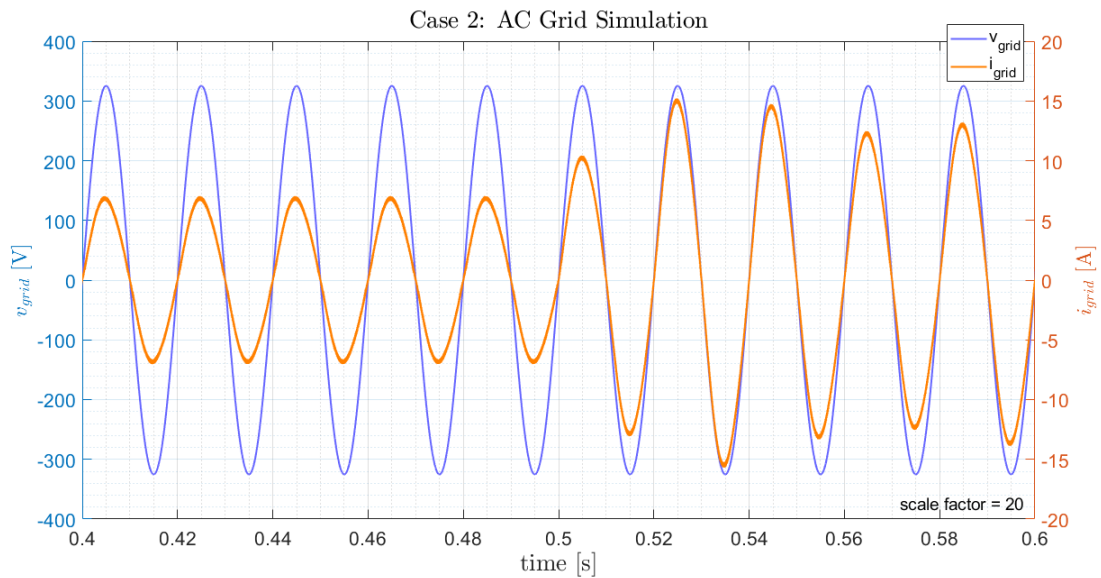
Figure 4.16: AC grid simulation results in case 2: voltage waveform (blue) and current waveform (orange).

It becomes clear, by analyzing figure 4.16, that at the instant the second load is connected to the DC grid, the value of the current increases, as expected. Besides, oscillations in the waveform of the current are also observed. The reason is that after the disturbance in the system (the connection of the second resistance), the system goes through a transient before reaching steady state. When the system reaches the steady-state again, the current stabilizes, and the previous oscillations are no longer observed, as shown in figure 4.17. This figure displays the voltage (blue) and current (orange) of the AC grid again, but this time in a time interval after reaching the steady-state regime with the two loads connected.
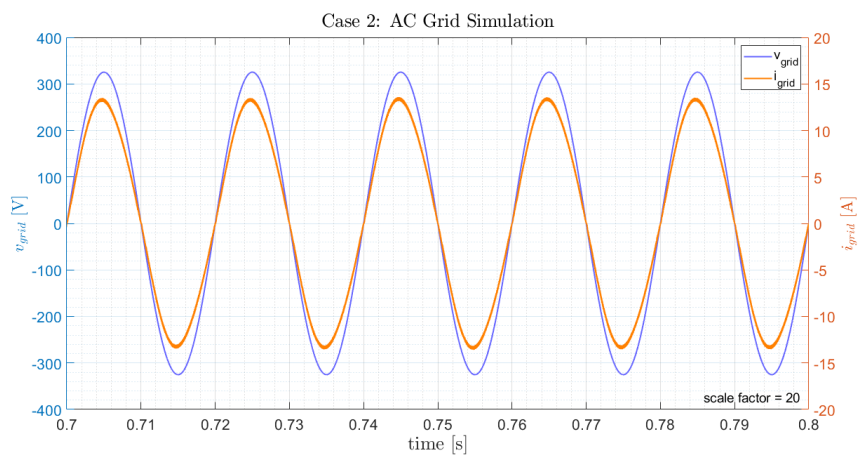
Figure 4.17: AC grid simulation results in case 2 in steady-state: voltage waveform (blue) and current waveform (orange).

Figure 4.18 shows the results of the DC grid simulation (the voltage in blue and the current in orange) at the moment the second load is switched on.
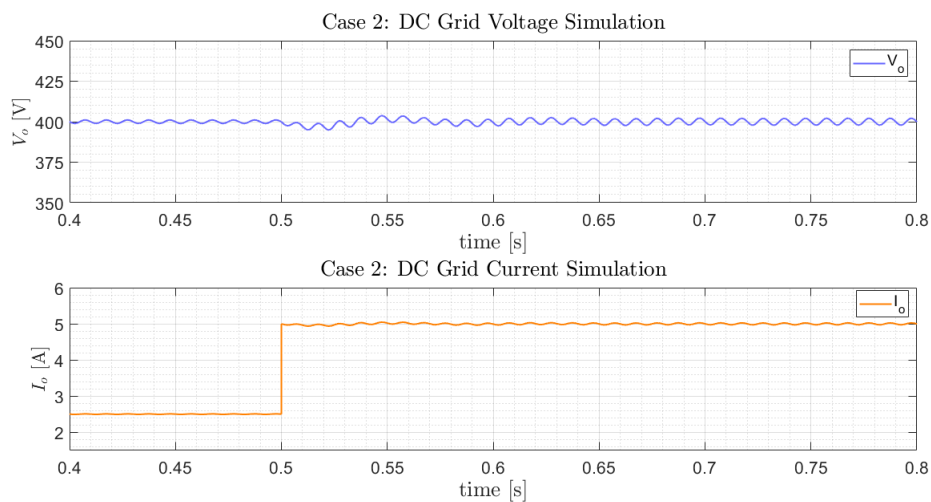

Figure 4.18: DC grid simulation results in case 2: voltage waveform (blue) and current waveform (orange).

It is evident from an analysis of figure 4.18 that once again, the results are in line with expectations. Since both the voltage and the current present an approximately constant waveform. However, it is possible to observe that at $t = 0.5$ s, the current value doubles, since from that moment, the load increases.

It can be verified that the small oscillations observed in the voltage waveform are nearly equal to the value defined in table 4.4. For this purpose, figure 4.19 shows the control errors of the V_o voltage (in blue) and i_L current (in orange) throughout the simulation.
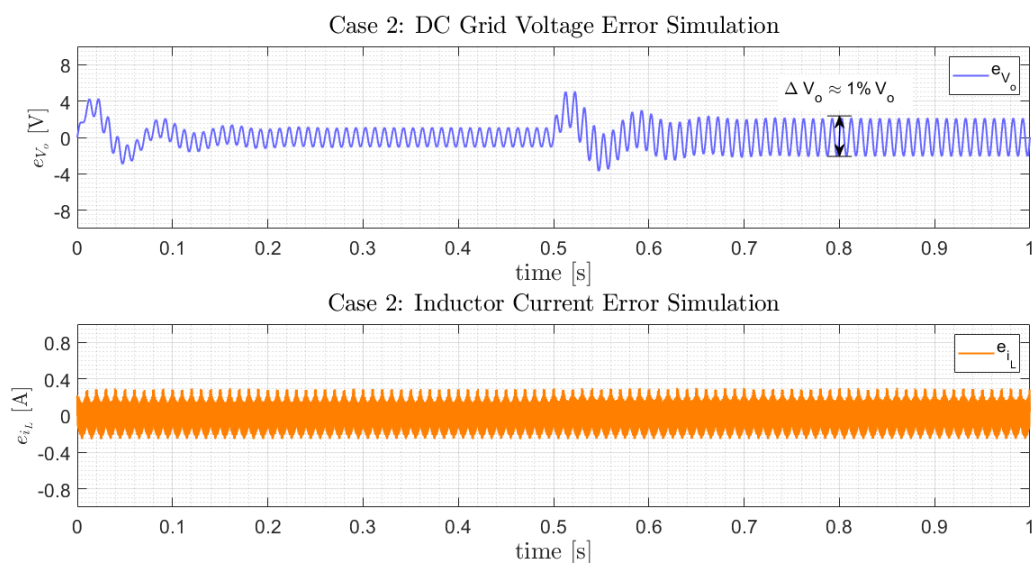
Figure 4.19: Control errors simulation results in case 2: DC grid voltage error (blue) and inductor current error (orange).

Based on the previous results it can be concluded that, in a stationary regime, the ripple of the V_o voltage presents an acceptable value and confirms that the results were good. Moreover, it is also evident from figure 4.19 that the control system defined allows controlling the i_L current properly.

4.2.3 DC Grid with a Constant Power Load

In this scenario, the DC network only has a CPL. Figure 4.20 shows the DC grid in this case, and it is possible to see that this grid consists of an input filter followed by a buck converter, which represents the CPL.
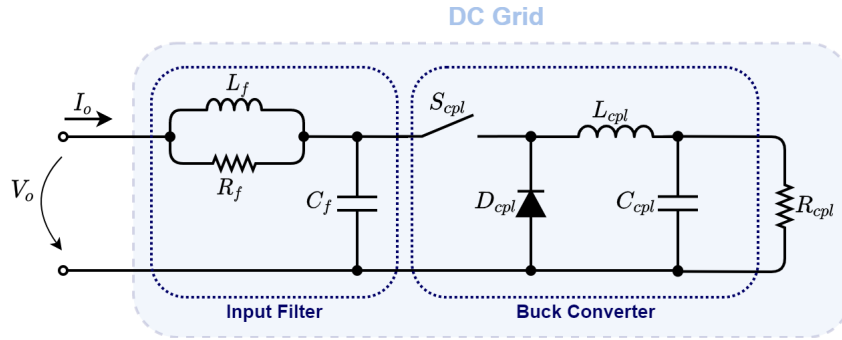
Figure 4.20: DC grid represented by a constant power load.

Tables 4.5 and 4.6 provide the numerical values of the CPL parameters and the input filter, respectively. From section 2.5.3, it is necessary to set the value of the cutting frequency, f_c, and the damping factor, ζ. In the case of the cut-off frequency, this should be one decade above 100 Hz, since the voltage on the DC side is rectified so, the frequency is twice the frequency of the AC grid (50Hz). Besides, it should be one decade below the switching frequency (50 kHz). Therefore, it was set f_c equal to 1 kHz, as indicated in table 4.6. On the other hand, the damping factor should be between 0.5 and 0.7, so it has been defined $\zeta = 0.6$.

Table 4.5: Constant Power Load parameters.

Constant Power Load

$V_{o_{cpl}}$ [V]	$P_{o_{cpl}}$ [kW]	f_s [kHz]	$\Delta i_{L_{cpl}}$	$\Delta V_{o_{cpl}}$	L_{cpl} [mH]	C_{cpl} [µF]	R_{cpl} [Ω]
400	2	50	$10\% \, i_{L_{cpl}}$	$1\% \, V_{o_{cpl}}$	18.0	0.278	80

Table 4.6: Input filter parameters.

Input Filter

f_c [kHz]	ζ	R_f [Ω]	L_f [mH]	C_f [µF]
1	0.6	45	8.594	2.947

To find out if the system operates with the desired values, the simulation results of both networks are presented below in this new scenario. In the case of the DC network, the results refer to its input (which corresponds to the filter input) and the output of the buck converter.

Figure 4.21 shows the results of the AC grid simulation in a time interval during the stationary regime, being the voltage represented in blue and the current in orange.
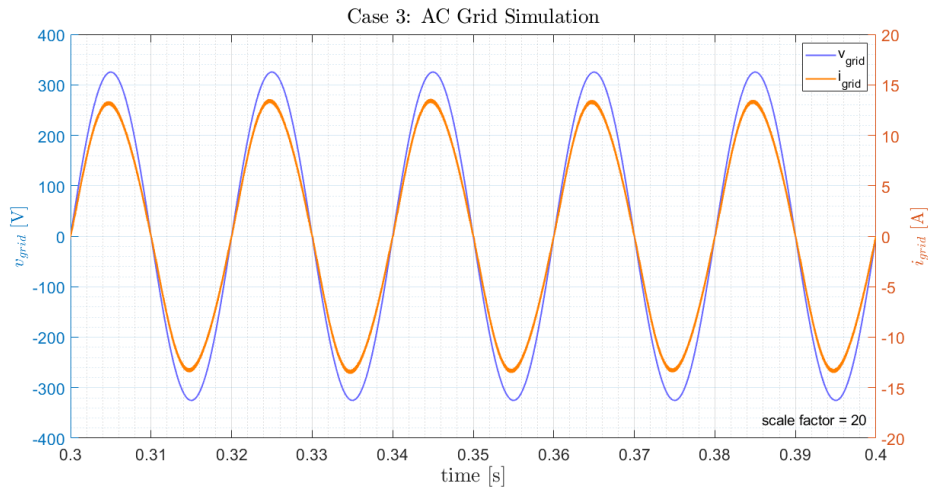
Figure 4.21: AC grid simulation results in case 3: voltage waveform (blue) and current waveform (orange).

By analyzing figure 4.21, it is possible to see that the results are similar to those previously obtained, that is, both the voltage and the current present sinusoidal waveforms. Therefore, it can be concluded that the results are again as expected.

Figure 4.22 shows the simulation results at the DC grid input, i.e., it displays in blue the V_o voltage in figure 4.20 and in orange the I_o current, also indicated in the same figure. The graphs present the results during the transient period and after the system reaches the steady-state.
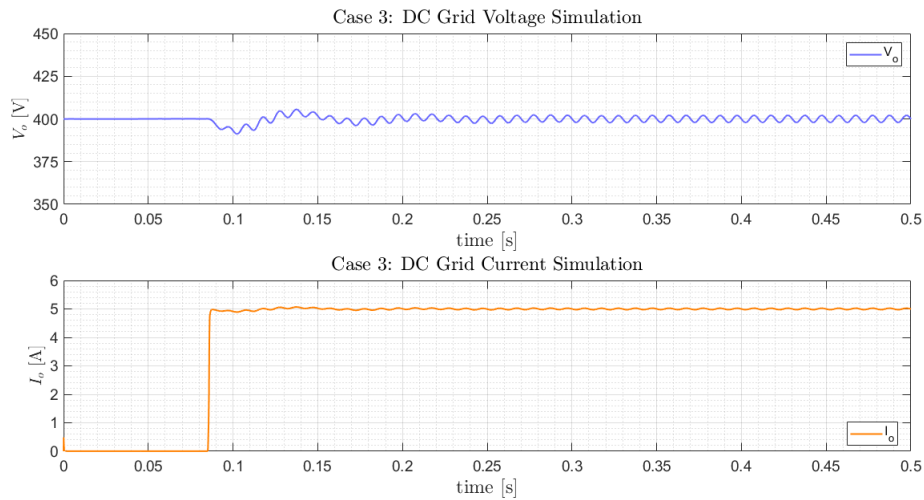
Figure 4.22: DC grid simulation results in case 3: voltage waveform (blue) and current waveform (orange).

Examining figure 4.22, it is clear that even with the inclusion of a CPL in the system, the results continue as expected since both the voltage and the current are approximately constant and present only a small ripple that is inevitable. However, it is necessary to check that the control system inserted

to control the step-down converter, which forms the CPL, is working correctly. That is if the $V_{o_{cpl}}$ voltage and $i_{L_{cpl}}$ current follow the respective references. Therefore, figure 4.23 introduces the results of the $V_{o_{cpl}}$ voltage simulation in blue and orange the $I_{o_{cpl}}$ current.
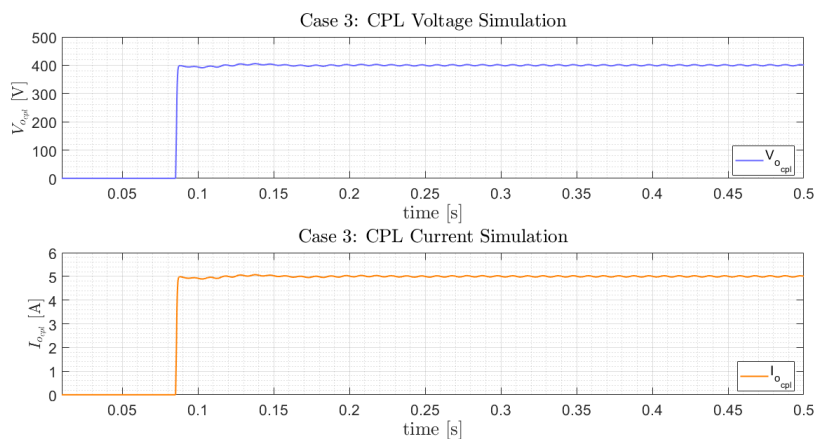
**Figure 4.23:** Constant Power Load's simulation results in case 3: voltage waveform (blue) and current waveform (orange).

By analyzing figure 4.23, it is possible to observe that the waveform of both signals is approximately constant, so it is evident that once more, the system presents the desired behavior.

To perform a fuller analysis, figure 4.24 shows the various control errors that make up the two non-linear control systems. Therefore, the upper graph shows the voltage control errors, where the e_{V_o} error is represented with a solid line, while the $e_{V_{o_{cpl}}}$ error is shown with a dashed line. On the other hand, the bottom graphic presents the current control errors, where the e_{i_L} error is represented in orange, and the $e_{i_{L_{cpl}}}$ error is in turquoise.
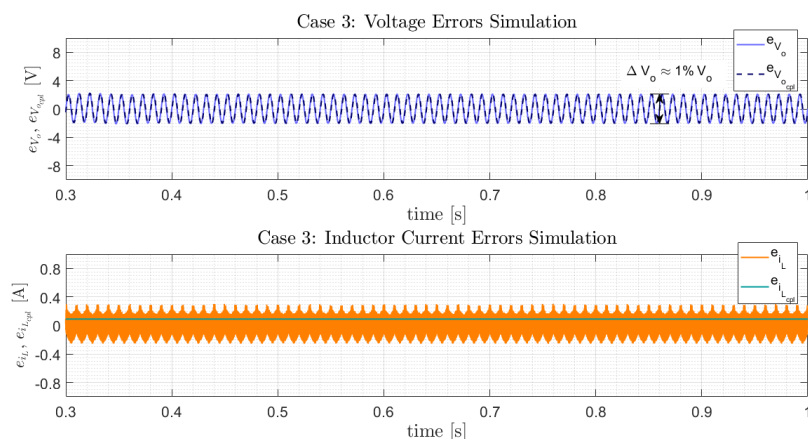
Figure 4.24: Control errors simulation results in case 3. Upper graph: DC grid voltage error (solid line) and CPL voltage error (dashed line). Lower graph: boost's inductor current error (orange) and buck's inductor current error (turquoise).

It is concluded that all the signs successfully follow the references because all the errors present results close to zero, considering the previous graphs. Furthermore, it is possible to verify that the ripples of the signals do not exceed the values defined during the sizing of the elements (tables 4.4 and 4.5). This way, it is proof that the system is working correctly.

4.2.4   DC Grid with a Current Source

The last study scenario aims to show one of the main characteristics of the system already mentioned, the bidirectional power flow that may result from the connection of a renewable power source, as a PV system, to the DC grid. In this way, a current source is added to the DC network to observe the change in the direction of the current, compared to the previous cases. Previously, the system had only one voltage source in the AC grid, and the current flowed from the AC grid to the DC grid. Now, the system has two sources (a voltage source on the AC grid and a current source on the DC grid), and the aim is to observe the current flowing in the opposite direction, that is, from the DC grid to the AC grid.

Therefore, the DC grid now consists of a parallel current source with a resistive load, R_o, as shown in figure 4.25, where R_o is equal to $80\,\Omega$. It is worth mentioning that the current source, I_{DC} is defined with a value equal to $2I_o$, i.e., 10 A.
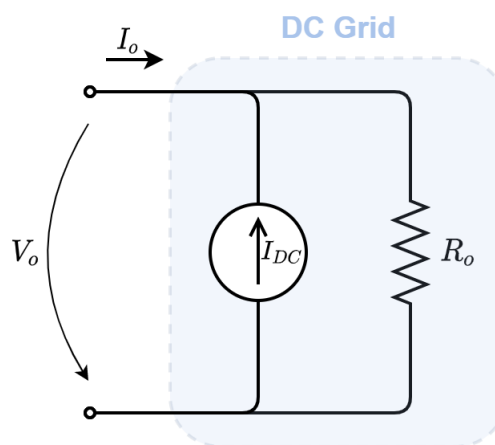
Figure 4.25: DC grid represented by a parallel current source with a resistor.

As in the previous cases, the simulation results of both networks are presented below, as well as the system control errors.

Figure 4.26 shows the simulation results of the AC grid voltage and current. As before, the voltage is represented in blue and the current in orange. Furthermore, figure 4.26a describes the response of the system during the transient period and figure 4.26b describes the response after the system has reached the steady-state.
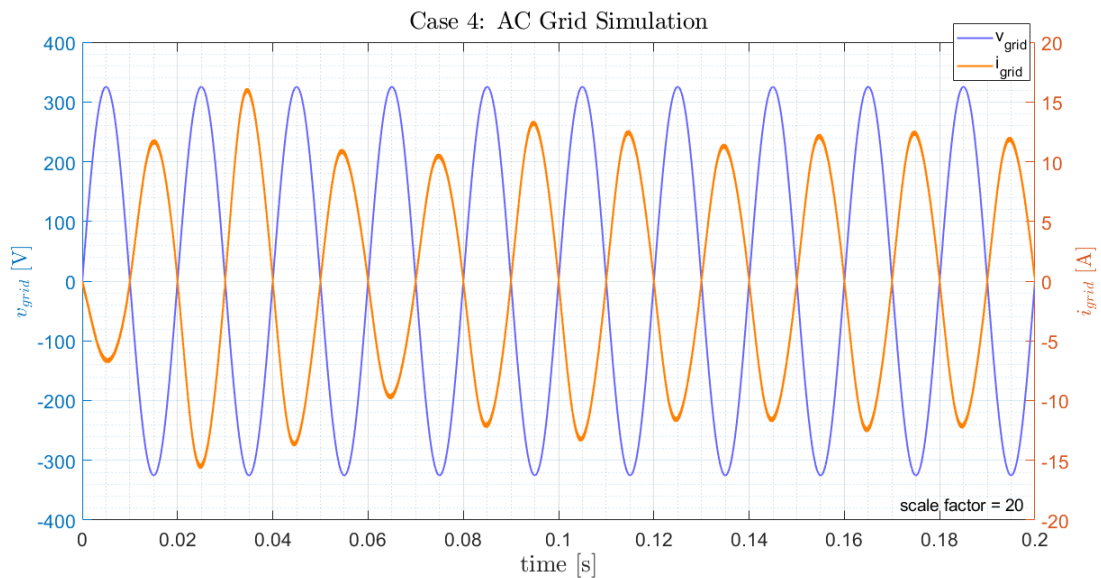
(a) Simulation results between 0 and 0.2 s.
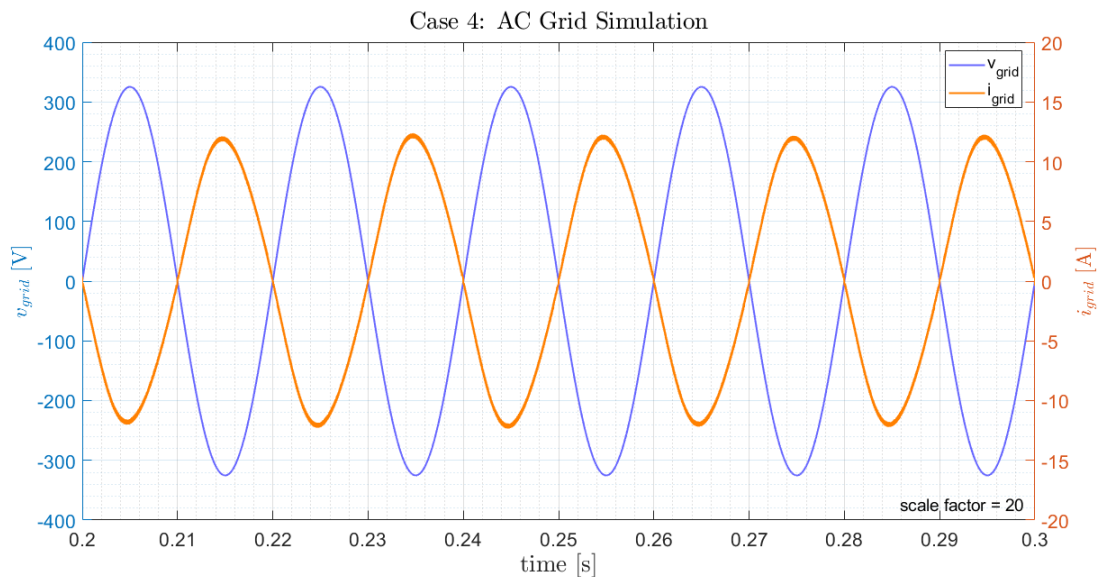
(b) Simulation results between 0.2 and 0.3 s.

Figure 4.26: AC grid simulation results in case 4: voltage waveform (blue) and current waveform (orange).

Analyzing figure 4.26, it is clear that the new results are different from those achieved previously. In this case, the voltage and current continue to present sinusoidal waveforms but are no longer in phase. They are now out of phase, which indicates that the current has changed direction. In other words, it

means that the goal of this case has been achieved, that is, it has been possible to show that the system allows bidirectional power flow. However, it is necessary to ensure that there no disturbances in the DC grid.

Figure 4.27 presents the results of the DC grid, with the voltage represented in blue and the current in orange.
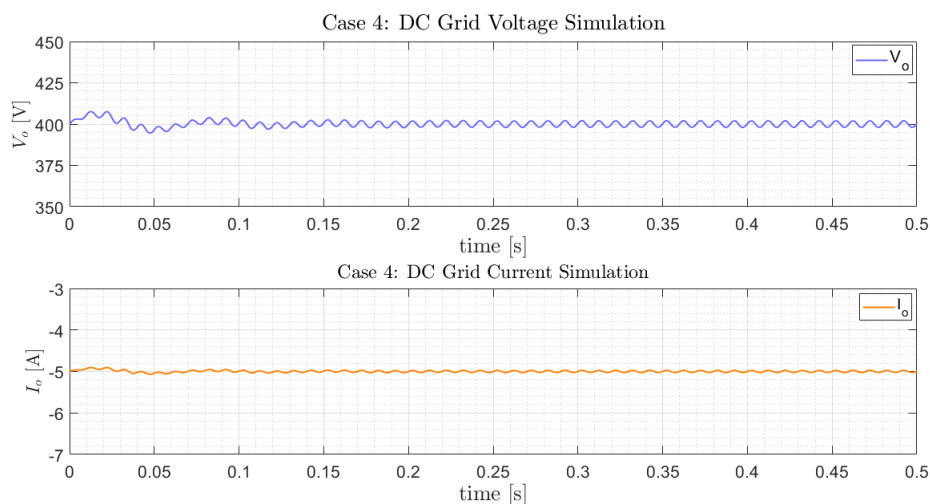
Figure 4.27: DC grid simulation results in case 4: voltage waveform (blue) and current waveform (orange).

Through the analysis of the waveforms in figure 4.27, it is clear once again that both DC voltage and DC current are approximately constant, after both reaching steady-state. However, the current presents a negative value, meaning that the current flows in the opposite direction compared to that established for its measuring device. It is noteworthy to point out that in all the simulations conducted within the scope of this dissertation, the measurement of the various signals took place in the direction indicated in the system diagrams presented in several figures, as in figure 4.1. In the case of I_o current, this was measured in the direction of the AC grid to the DC grid, as shown in figure 4.25. Consequently, if, in this case, the current presents a negative value, it means that is flowing from the DC network to the AC network, thereby proving that the system is bidirectional.

Finally, it is presented the control errors to show that the ripple of the V_o voltage does not exceed the value established during the sizing of the components after the system reaches the steady-state. Therefore, figure 4.28 presents in blue the control error of the V_o voltage and in orange the control error of the i_L current. By analyzing this figure, it can be seen that the V_o ripple is approximately 1% of V_o, so it presents a reasonable value, and it is proved that the system is working correctly.
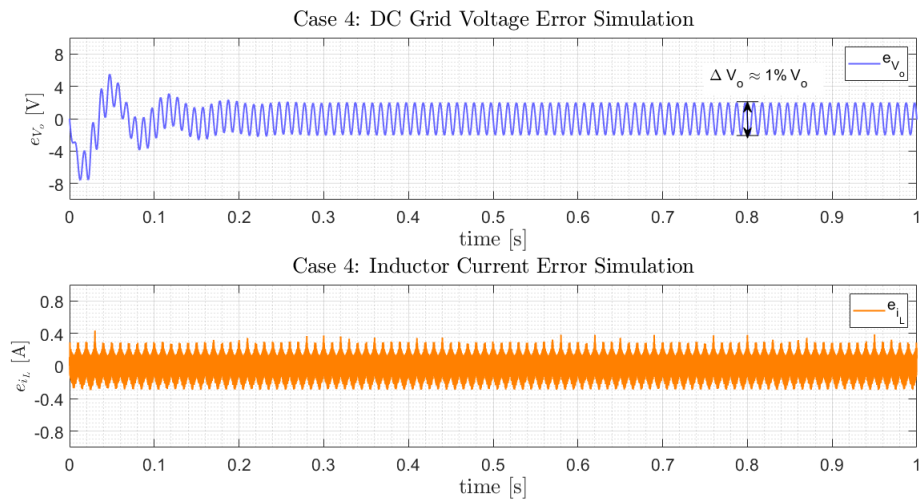
Figure 4.28: Control errors simulation results in case 4: DC grid voltage error (blue) and inductor current error (orange).

5

Conclusion

Contents

5.1   Final Conclusions

This dissertation focuses on the study of a single-phase, bi-directional, and isolated AC/DC converter that allows connecting a low voltage AC grid to a DC grid. In this way, it is possible to create a hybrid network, that when compared to the existing AC network, allows reducing the number of conversions and consequently increase the overall efficiency of the system and reduce its losses.

It is proposed a conversion system containing an AC/AC matrix converter that allows converting the AC grid voltage, at 50 Hz, into a sinusoidal voltage, switching at 50 kHz. This converter is then connected to a HFT, thus guaranteeing galvanic isolation using a transformer with considerably smaller dimensions when compared to a conventional 50 Hz transformer. The secondary side of the HFT is connected an AC/DC matrix converter. This converter aims to convert the 50 kHz sinusoidal signal into a 50 Hz rectified sinusoidal voltage, allowing bidirectional power flow. The last component is a DC/DC step-up converter that aims to convert the voltage of the AC/DC converter output into a constant voltage that allows the correct operation of the DC network. After a detailed study of the proposed system, the components of the various elements are sized, and the command signals of the matrix converters are defined, considering the role each one has in the system.

A non-linear control system is developed to ensure that the conversion system does not create disturbances in the AC and DC networks. This controller is based on the Backstepping and sliding mode control theories and consists of two loops. The external loop allows controlling the DC grid voltage while the internal loop ensures that the DC/DC converter inductor current follows its reference.

Through the analysis of the results of the simulations, we realize that the proposed solution presents an adequate response in different scenarios. These scenarios differ from each other by the structure of the DC network, which starts by having a simple architecture with only one resistive load and then with two resistive loads in parallel. The third case considers a DC network constituted by a CPL. In this case, it is necessary to size and to design controllers for the CPL.

The conclusions reached in all three cases are identical and confirm that the system meets the requirements. This means that both the voltage and the current of the AC grid present sinusoidal waveforms, without disturbances, as was desired. On the other hand, the current and voltage of the DC grid have approximately constant waveforms, and there is a small ripple in both waveforms, but it is considered acceptable. Regarding the control system, in all cases, the voltages and currents to be controlled follow the respective references since the control errors have small values.

The last scenario presents the DC network constituted by a current source and has a specific objective, to demonstrate that the system is bidirectional. The results of this scenario prove that the system is bi-directional because there is a change in the direction of power flow. This change in direction is visible in the AC network and DC network results. In the AC grid, it is verified that the current and voltage are out of phase. On the other hand, on the DC network, the current has a negative value, which means

that the current flows in the opposite direction to the one being measured, thus proving that the system is bi-directional.

An analysis of the work developed in this dissertation concludes that the proposed conversion system meets all the requirements.

5.2 Future Work

Although the proposed system achieves all the proposed objectives, this system can still be improved. Therefore, it is suggested that for future research, it would be interesting to develop a model closer to reality. This new model could consider more complex DC grid scenarios, such as several CPL loads in parallel, the replacement of the current source by a renewable energy source, for example, a photovoltaic system, or even consider a more complex AC network with the inclusion of AC loads.

This dissertation performed only a study based on simulations. An improvement would be to build a prototype in the laboratory and therefore conduct a more reliable evaluation of the system.

Additionally, another suggestion to complement the work already done is to perform an analysis that allows comparing this solution with other more conventional typologies, with the inclusion of a comparative study in terms of volume and efficiency of the systems.

Finally, it is suggested that an economic evaluation of the proposed solution be conducted because besides having a system that presents successful results, the project must be economically viable.

Bibliography

[1] David, P. A.; Bunn, J. A. The economics of gateway technologies and network evolution: Lessons from electricity supply history. *Information economics and policy*, 1988, 3.2: 165-202.

[2] Wang, P., et al. Harmonizing AC and DC: A hybrid AC/DC future grid solution. *IEEE Power and Energy Magazine*, 2013, 11.3: 76-83.

[3] Paraíso, G. M.; Pinto, S. F.; Silva, J. F. Modelling and nonlinear control of Dual-Active Bridge converters for DC microgrids. In: IECON 2019-45th *Annual Conference of the IEEE Industrial Electronics Society*. IEEE, 2019. p. 1850-1855.

[4] Liu, X.; Wang, P.; Loh, P. C. A hybrid AC/DC microgrid and its coordination control. *IEEE Transactions on smart grid*, 2011, 2.2: 278-286.

[5] Flaticon, available online: www.flaticon.com (last acess: 30.10.2020)

[6] Everts, J. Modeling and optimization of bidirectional dual active bridge ac-dc converter topologies. *ARENBERG DOCTORAL SCHOOL FACULTY OF ENGINEERING SCIENCE,* 2014.

[7] Van der Merwe, J. W.; Mouton, H. du T. The solid-state transformer concept: A new era in power distribution. In: *AFRICON 2009.* IEEE, 2009. p. 1-6.

[8] Gonzalez-Garcia, C.; Pleite, J. Transformer model in wide frequency bandwidth for power electronics systems. *Advances in Power Electronics*, 2013, 2013.

[9] Bhattacharya, S., et al. Design and development of generation-I silicon based solid state transformer. In: *2010 Twenty-Fifth Annual IEEE Applied Power Electronics Conference and Exposition (APEC).* IEEE, 2010. p. 1666-1673.

[10] Fan, H.; Li, H. High-frequency transformer isolated bidirectional DC–DC converter modules with high efficiency over wide load range for 20 kVA solid-state transformer. *IEEE Transactions on Power Electronics*, 2011, 26.12: 3599-3608.

[11] Pinto, S. F.; Mendes, P. V.; Silva, J. F. Modular matrix converter based solid state transformer for smart grids. *Electric Power Systems Research*, 2016, 136: 189-200.

[12] She, X.; Huang, A. Q.; Burgos, R. Review of solid-state transformer technologies and their application in power distribution systems. *IEEE journal of emerging and selected topics in power electronics*, 2013, 1.3: 186-198.

[13] Fernandes, P. Transformador Electrónico de Potência para Aplicações em Sistemas de Energia. *Instituto Superior Técnico, Dissertação de Mestrado Integrado em Engenharia Electrotécnica e de Computadores*, 2014.

[14] Paiva, J. Redes de energia elétrica. Uma análise sistémica, 3a. 2011.

[15] Idris, Z.; Noor, SZ M.; Hamzah, M. K. Safe commutation strategy in single phase matrix converter. In: *2005 International Conference on Power Electronics and Drives Systems*. IEEE, 2005. p. 886-891.

[16] Wheeler, P. W., et al. Matrix converters: A technology review. *IEEE Transactions on industrial electronics,* 2002, 49.2: 276-288.

[17] Silva, J. F.; Pinto, S.; Santana, J. Conversores Comutados para Energias Renováveis. *Support text, IST*, 2013.

[18] Van Der Merwe, J. J. *Method of Amplitude Modulating a Message Signal in the Audible Frequency Range Onto a Carrier Signal in the Ultrasonic Frequency Range.* U.S. Patent Application No 12/065,162, 2008.

[19] Idris, Z.; Hamzah, M. K.; Saidon, M. F. Implementation of single-phase matrix converter as a direct ac-ac converter with commutation strategies. In: *2006 37th IEEE Power Electronics Specialists Conference*. IEEE, 2006. p. 1-7.

[20] Nikkhajoei, H. A current source matrix converter for high-power applications. In: *2007 IEEE Power Electronics Specialists Conference*. IEEE, 2007. p. 2516-2521.

[21] Hasaneen, B. M.; Mohammed, A. A. E. Design and simulation of DC/DC boost converter. In: *2008 12th International Middle-East Power System Conference*. IEEE, 2008. p. 335-340.

[22] Singh, S.; Gautam, A. R.; Fulwani, D. Constant power loads and their effects in DC distributed power systems: A review. *Renewable and Sustainable Energy Reviews*, 2017, 72: 407-421.

[23] Di Bernardo, M.; Budd, C.; Champneys, A. Grazing, skipping and sliding: analysis of the non-smooth dynamics of the DC/DC buck converter. Nonlinearity, 1998, 11.4: 859.

[24] Wei, X.; Tsang, K. M.; Chan, W. L. DC/DC buck converter using internal model control. *Electric Power Components and Systems*, 2009, 37.3: 320-330.

[25] Johansson, B. DC-DC converters-dynamic model design and experimental verification. Lund University, 2005.

[26] Silva, J. F. Input filter design for power converters. In: *Lecture notes*. IST, 2012.

[27] Pinto, S. F.; Silva, J. F. Input filter design of a mains connected matrix converter. In: *Proceedings of the IEEE 12th ICHQP International Conference on Harmonics and Quality of Power*, Cascais, Portugal. 2006. p. 1-6.

[28] Bailey, F. N. The application of Lyapunov's second method to interconnected systems. *Journal of the Society for Industrial and Applied Mathematics, Series A: Control*, 1965, 3.3: 443-462.

[29] Kalman, R. E.; Bertram, J. E. Control system analysis and design via the "second method" of Lyapunov: I—continuous-time systems. 1960.

[30] Zhang, S., et al. Dynamic backstepping control for pure-feedback non-linear systems. *IMA Journal of Mathematical Control and Information*, 2020, 37.2: 670-693.

[31] Kokotovic, P. V. The joy of feedback: nonlinear and adaptive. *IEEE Control Systems Magazine*, 1992, 12.3: 7-17.

[32] Martin, A. D., et al. Backstepping control of smart grid-connected distributed photovoltaic power supplies for telecom equipment. IEEE transactions on energy conversion, 2015, 30.4: 1496-1504.

[33] Young, K. D.; Utkin, V. I.; Ozguner, U. A control engineer's guide to sliding mode control. *IEEE transactions on control systems technology*, 1999, 7.3: 328-342.

[34] Utkin, V. I. Sliding mode control design principles and applications to electric drives. *IEEE transactions on industrial electronics*, 1993, 40.1: 23-36.

[35] Da Silva, J. F. A., et al. Advanced control methods for power electronics systems. *Mathematics and computers in simulation*, 2003, 63.3-5: 281-295.

[36] Shah, D. H.; Mehta, A. Preliminaries of Sliding Mode Control and Networked Control System. In: *Discrete-Time Sliding Mode Control for Networked Control System*. Springer, Singapore, 2018. p. 19-35.

[37] Hasaneen, B. M.; Mohammed, A. A. E. Design and simulation of DC/DC boost converter. In: *2008 12th International Middle-East Power System Conference*. IEEE, 2008. p. 335-340.

A

Sizing of the High-Frequency Transformer

The following is a detailed description of the sizing used in the characterization of the High-Frequency Transformer elements.

Table A.1 shows the nominal values of a conventional transformer (50 Hz), both in the SI units and in p.u. values.

Table A.1: Nominal values of the transformer.

		SI units	p.u. values
U_n	Primary voltage [V]	230	1
	Secondary voltage [V]	230	1
P_n	Nominal Power [VA]	2000	1
I_n	Primary current [A]	5	1
	Secondary current [A]	5	1

It is worth mentioning that the p.u. values present in table A.1 take into consideration the bases defined by expression (A.1).

$$\begin{cases} S_b &= P_n \\ U_b &= U_n \\ I_b &= I_n = \frac{P_n}{\sqrt{3}U_n} \\ Z_b &= \frac{U_b^2}{S_b} \end{cases} \tag{A.1}$$

Table A.2 presents the results of the no-load and short-circuit transformer tests.

Table A.2: Results of the no-load and short-circuit transformer tests.

No-load test	P_o	No-load power	$0.5\% \, P_n$	0.005 p.u.
	I_m	Magnetizing current	$3\% \, I_n$	0.03 p.u.
Short circuit test	P_{sc}	Short circuit power	$0.8\% \, P_n$	0.008 p.u.
	U_{sc}	Short circuit voltage	$1\% \, U_n$	0.01 p.u.

From the no-load test values, it is possible to define the magnetization conductance, G_m, and magnetization susceptance, B_m, from expressions (A.2) and (A.3). These, in turn, allow the definition of magnetization resistance, R_m, and magnetization inductance, L_m, through the expression (A.4).

$$G_m = \frac{P_o}{U_n^2} \Rightarrow G_{m_{pu}} = P_{o_{pu}} \tag{A.2}$$

$$B_m = \sqrt{\left(\frac{I_m}{U_n}\right)^2 - G_m^2} \Rightarrow B_{m_{pu}} = \sqrt{I_{m_{pu}}^2 - G_{m_{pu}}^2} \tag{A.3}$$

$$\begin{cases} R_m &= \frac{1}{G_m} \\ L_m &= \frac{1}{2\pi 50 B_m} \end{cases} \tag{A.4}$$

On the other hand, the results of the short circuit test allow the definition of the winding resistances, R_{T1} and R_{T2}, and the leakage reactance, X_T, taking into account the expressions (A.5) and (A.6).

72

$$R_{T1} = R_{T2} = \frac{1}{2}\frac{P_{sc}}{I_n^2} \Rightarrow R_{T1_{pu}} = R_{T2_{pu}} = \frac{1}{2}P_{sc_{pu}} \tag{A.5}$$

$$X_T = \sqrt{\left(\frac{U_{sc}}{I_n}\right)^2 - R_T^2} \Rightarrow X_{T_{pu}} = \sqrt{U_{sc_{pu}}^2 - R_{T_{pu}}^2} \tag{A.6}$$

In case this transformer was a conventional one, the inductances of the copper windings, L_{T1} and L_{T2}, were defined by expression (A.7). However, this is a high-frequency transformer, so it is necessary to correct these parameters due to the working frequency. Therefore, expression (A.8) includes the equation used to size the inductances L_{T1} and L_{T2}.

$$L_{T1} = L_{T2} = \frac{1}{2}\frac{X_T}{2\pi 50} \tag{A.7}$$

$$L_{T1} = L_{T2} = \frac{1}{2}\frac{X_T}{f_s} \tag{A.8}$$

Matlab's Simulink simulation program is used to perform the different scenarios. In this program, the transformer is represented by its T diagram. However, the base defined for the inductances is not the same as the resistances, so it is necessary to change the base in these cases. Therefore, expression (A.9) presents the base used by Simulink for the inductances, while expression (A.10) provides the equation to perform the base change.

$$L_b = \frac{Z_b}{2\pi f_s} \tag{A.9}$$

$$L'_{pu} = L_{SI}\frac{Z_b}{L_b} \tag{A.10}$$

Table A.3 presents the values of the HFT elements reached through this sizing.

Table A.3: High Frequency Transformer parameters.

	R_{T1} [Ω]	R_{T2} [Ω]	L_{T1} [μF]	L_{T2} [μF]	R_m [kΩ]	L_m [F]
	0.106	0.106	1.587	1.587	5.290	2.846
p.u.	0.004	0.004	0.019	0.019	200	$3.381e^4$

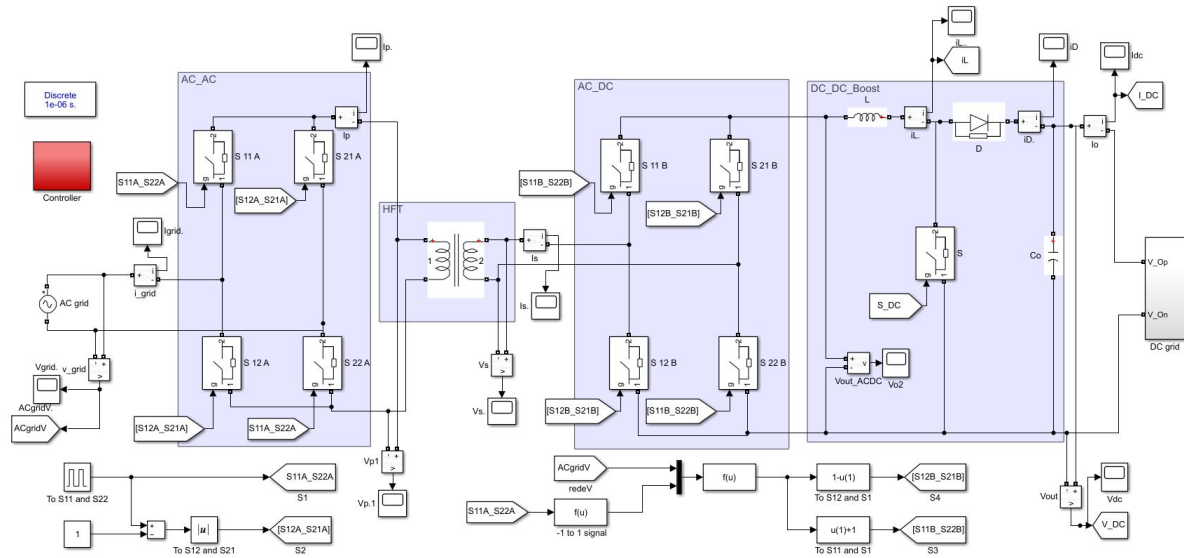# B

Simulation Diagrams

In this appendix, all the simulation schemes used in the Simulink program to simulate the system in the four cases are shown.

Figure B.1 provides the schematic showing all the elements of the system, and which is used in scenarios 1, 2, and 4.

Figure B.1: Global diagram of the system used in cases 1, 2, and 4.
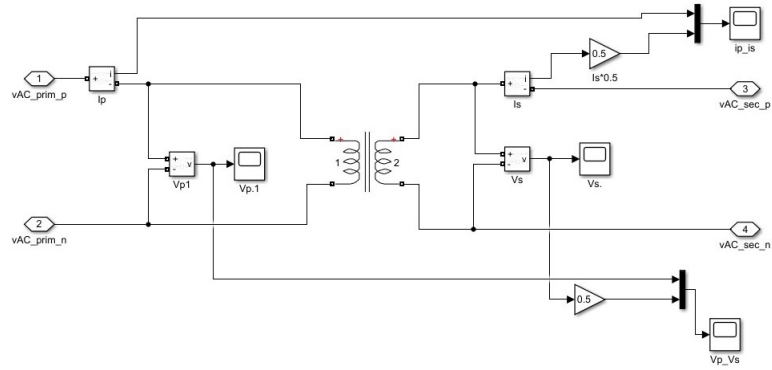
Figures B.2, B.3, and B.4 present the diagrams of the matrix converters, the HFT, and the boost converter, respectively, being these elements that compose the system in all cases of study.
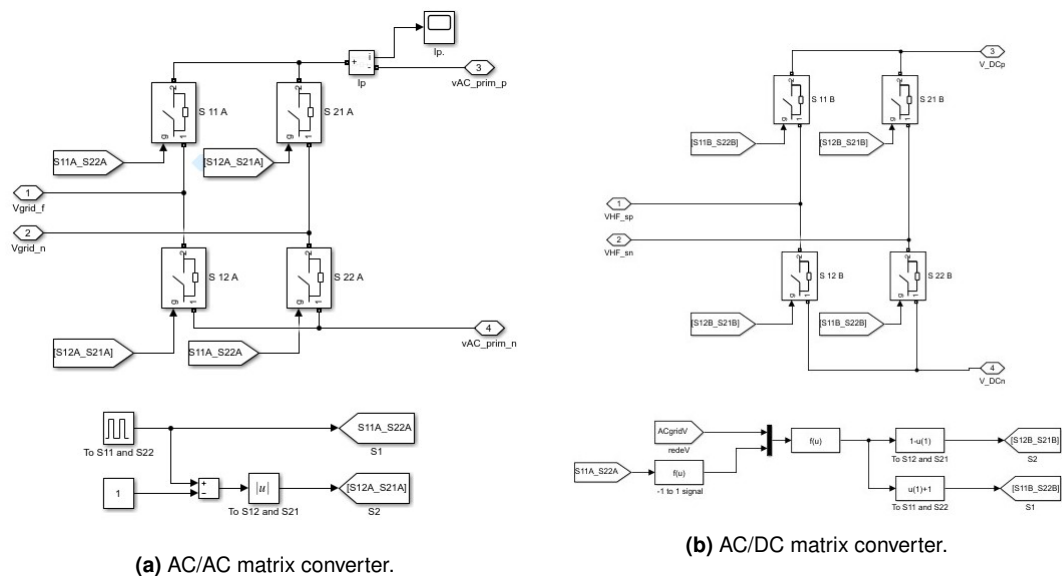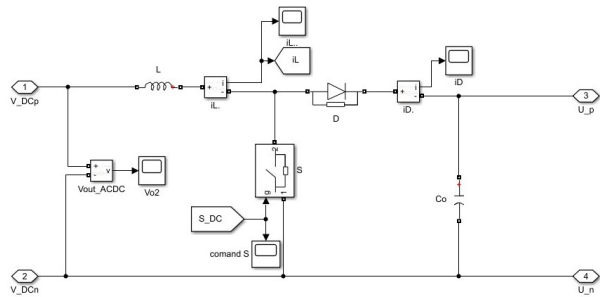

(a) AC/AC matrix converter.

(b) AC/DC matrix converter.

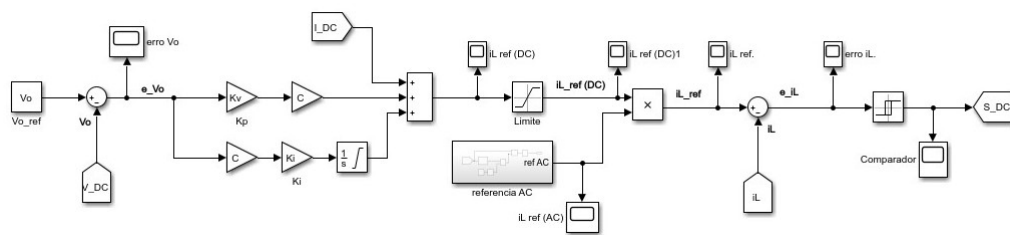**Figure B.2:** Diagram of the matrix converters.

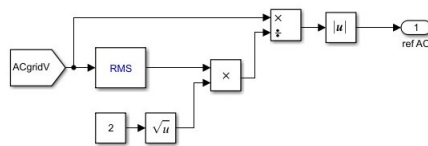**Figure B.3:** Diagram of High Frequency Transformer.

Figure B.4: Diagram of step-up converter.

Figure B.5 presents the scheme of the system control system, while figure B.6 displays the subsystem with the name *"referencia AC"* in figure B.5.
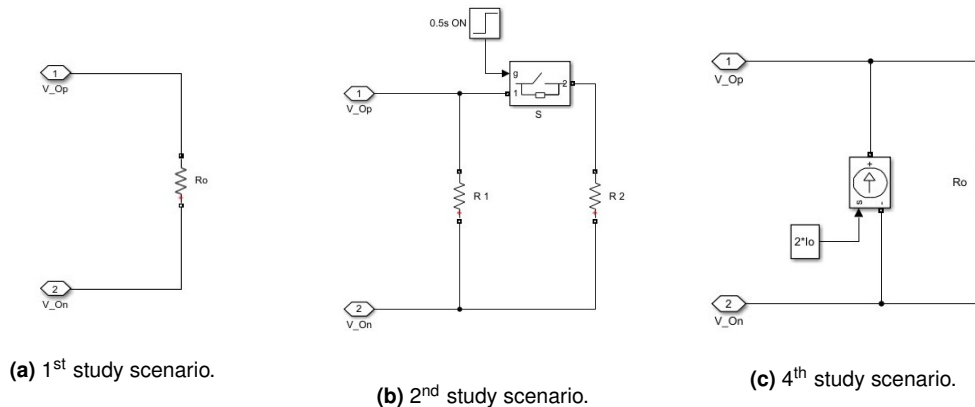

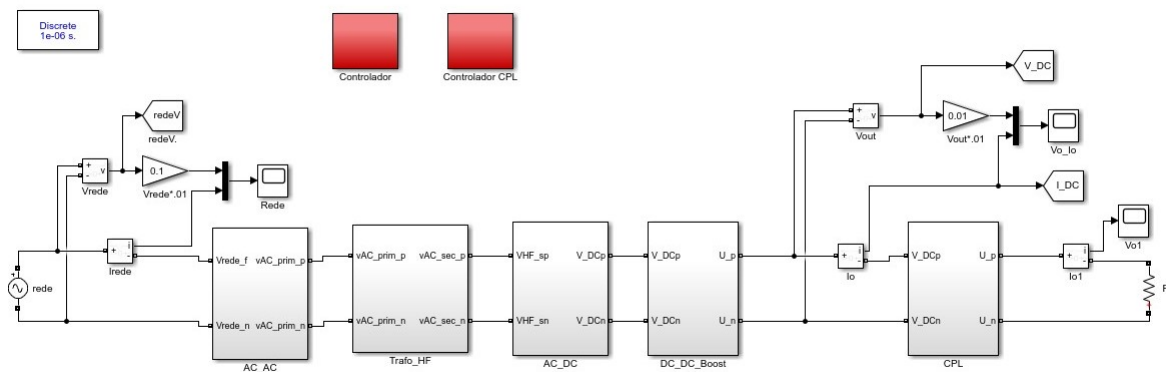**Figure B.5:** Diagram of the control system.

Figure B.6: Diagram of *"referencia AC"* subsystem (presents in figure B.5.

Figure B.7 illustrates the DC network configuration in cases 1 (figure B.7a), 2 (figure B.7b), and 4 (figure B.7c).

(a) 1$^{\text{st}}$ study scenario.

(b) 2$^{\text{nd}}$ study scenario.

(c) 4$^{\text{th}}$ study scenario.

Figure B.7: Diagram of the DC network in the different study scenarios.

Figures B.8, B.9, and B.10 present the system schemes that have changed with the inclusion of the CPL, the third case study. Therefore, figureB.8 presents the overall diagram of the system, figure B.9, the diagram of the buck converter and the input filter, and finally, figure B.10, the control system diagram of the step-down converter.

Figure B.8: Global diagram of of the system used in case 3.
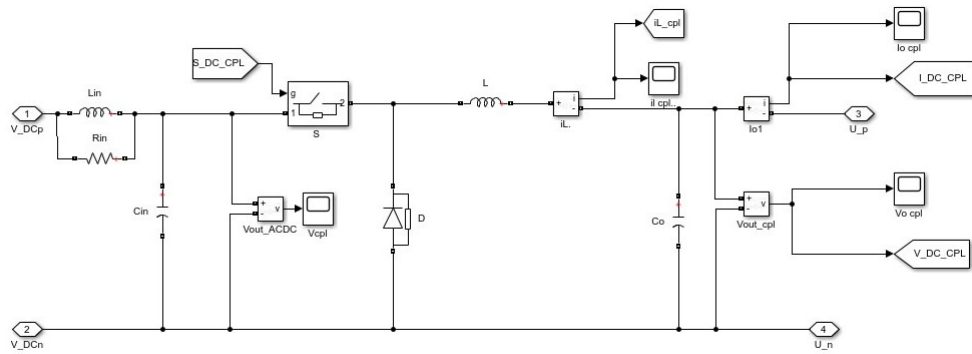
Figure B.9: Diagram of step-down converter with the input filter.
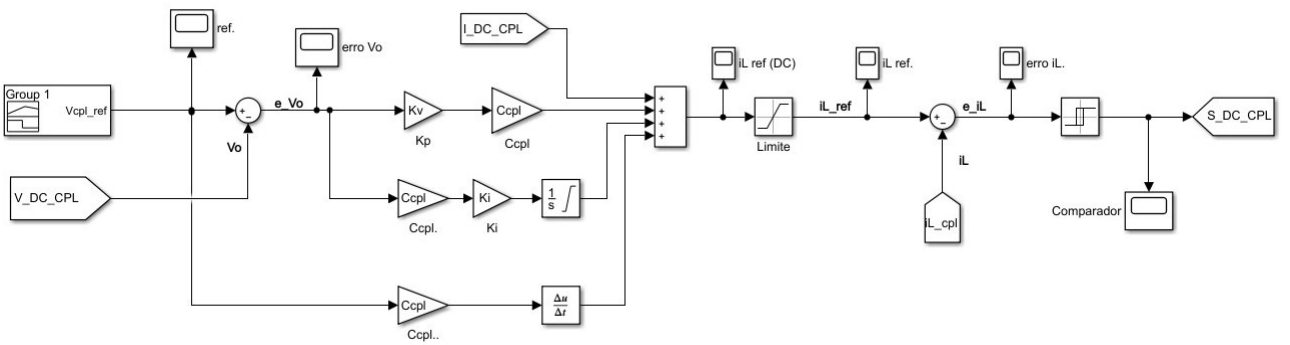
Figure B.10: Diagram of the buck converter control system.

C

Simulation Data

This annex contains the Matlab code used to sizing the elements that make up the simulation system.

```matlab
1  %--------------------------------------------
2  %  Simulation Data / Dados de simulacao
3  %--------------------------------------------
4
5  close all;
6  clear all;
7  clc
8
9  % Rede
10 redeVrms = 230;              % em V
11 redeVmax = sqrt(2)*redeVrms; % em V
12 redeFase = 0;
13 redef = 50;                  % em Hz
14 redeT = 1/redef;             % em s
15 w_rad = 2*pi*redef;          % em rad/s
16
17 % Conversor AC/AC
18 Fcum = 50*10^3;              % em Hz
19 Tcum = 1/Fcum;               % em s
20 delayS12 = Tcum/2;           % em s
21
22 % Dimensionamento do transformador
23 P = 2*10^3;                  % Pn (VA)
24 m = 1;                       % relacao
25 Un = redeVrms;               % V nominal (V)
26 In = P/(sqrt(3)*Un);         % I nominal (A)
27
28 %---Vazio---
29 Xf.Po = 0.5*P/100 ;          % considerando 0.5% de Pn
30 Xf.Io = 0.03*In;             % considerando  3% de In
31 %---C.C-----
32 Xf.Ucc = 1*Un/100;           % considerando   1% de Un
33 Xf.Pcc = 0.8*P/100;          % considerando 0.8% de Pn
34 %---Valores base----
35 Xf.Base.Sb = P;
36 Xf.Base.Ib = In;
```

```matlab
37  Xf.Base.Ub = Un;

38  Xf.Base.Zb = Un^2/Xf.Base.Sb;

39  %-------Para pu--------------

40  Xf.PU.Po = Xf.Po/Xf.Base.Sb;

41  Xf.PU.Up = Un/Xf.Base.Ub;

42  Xf.PU.Pcc = Xf.Pcc/Xf.Base.Sb;

43  Xf.PU.In = In/Xf.Base.Ib;

44  Xf.PU.Ucc = Xf.Ucc/Xf.Base.Ub;

45  Xf.PU.Im = Xf.Io/Xf.Base.Ib;

46

47  % calculos dos parametros

48  Xf.PU.Gm = Xf.PU.Po/Xf.PU.Up;

49  Xf.PU.Rm = 1/Xf.PU.Gm;

50  Xf.PU.Bm = -sqrt((Xf.PU.Im/Xf.PU.Up)^2-Xf.PU.Gm^2);

51  Xf.PU.Xm = 1/Xf.PU.Bm*(-1);

52  Xf.PU.Zcc = Xf.PU.Ucc/Xf.PU.In;

53  Xf.PU.Rt = Xf.PU.Pcc/Xf.PU.In^2;

54  Xf.PU.Xt = sqrt(Xf.PU.Zcc^2-Xf.PU.Rt^2);

55

56  %-enrolamento primario

57  Up = Un;                    %V1(Vrms)

58  RT1pu = Xf.PU.Rt/2;         %R1(pu)

59  LT1pu = Xf.PU.Xt/2;         %L1(pu)

60  %-enrolamento secundario

61  Us = Un;                    %V2(Vrms)

62  RT2pu = Xf.PU.Rt/2;         %R2(pu)

63  LT2pu = Xf.PU.Xt/2;         %L2(pu)

64  %-ramo de magnetizacao

65  Rmpu = Xf.PU.Rm;            %(pu)

66  Lmpu = Xf.PU.Xm/w_rad;      %(pu)

67

68  %Correcaoo dos Parametros face a Alta frequencia %%%%

69  % %-enrolamento primario

70  LT1pu = LT1pu/(Fcum);       %L1(pu)

71  %-enrolamento secundario

72  LT2pu = LT2pu/(Fcum);       %L2(pu)

73

74  % converter para SI
```

```matlab
75  RT1si = RT1pu*Xf.Base.Zb;

76  RT2si = RT2pu*Xf.Base.Zb;

77  LT1si = LT1pu*Xf.Base.Zb;

78  LT2si = LT2pu*Xf.Base.Zb;

79  Rmsi = Rmpu*Xf.Base.Zb;

80  Lmsi = Lmpu*Xf.Base.Zb;

81

82  % Mudanca de base (Xbase ->Lbase)

83  LT1pu = LT1pu*2*pi*Fcum;

84  LT2pu = LT2pu*2*pi*Fcum;

85  Lmpu = Lmpu*2*pi*Fcum;

86

87  % Dimensionar BOOST

88  wcum = 2*pi*Fcum;          % em rad/s

89  Vo = 400;                  % em V

90  Ro = Vo^2/P;               % em ohm

91  Io = P/Vo;                 % em A

92

93  iL = P/Us;                 % em A

94  L = Vo*Tcum/(4*0.1*iL);    % em H

95

96  C = P/(w_rad*Vo*0.01*Vo);  % em F

97

98  % Dimensionar controlador

99  Kv = 80;

100 Ki = 20e3;

101

102 %-------CPL-----------------

103 % Dimensionar Buck

104 Pcpl = 1000;                      % em w

105 Vocpl = 300;                      % em V

106 iLcpl = Pcpl/Vocpl;               % em A

107

108 Rcpl = Vocpl^2/Pcpl;                      % em ohm

109 Lcpl = Vocpl*Tcum/(0.1*iLcpl);            % em H

110 Ccpl = (Vocpl*Tcum^2)/(0.01*Vocpl*8*Lcpl); % em F

111

112 % input filter
```

```matlab
113  wcorte = 1e3*2*pi;
114  Coef_amort = 0.6;
115  Ri = -(Vocpl^2/Pcpl);
116  Zf = -Coef_amort*Ri;
117  Rin = Zf/(2*Coef_amort);
118  Cin = 1/(Zf*wcorte);
119  Lin = Zf/wcorte;
```